www.pss-b.com

Progress, Challenges, and Rewards in Probing Melt Dynamics, Configurational Entropy Change, and Topological Phases of Group V- and Group IV-Based Multicomponent Sulfide Glasses

*Soumendu Chakravarty, Badriah S. Almutairi, Ralph Chbeir, Shibalik Chakraborty, Mathieu Bauchy, Matthieu Micoulaut, and Punit Boolchand**

The observation of reversibility windows (RWs) in binary Ge_xS_{100-x}, As_xS_{100-x} and ternary $Ge_xAs_xS_{100-2x}$ glass systems permits constructing a global topological phase diagram in the Ge—As—S composition triangle. The RW denotes glass compositions for which the enthalpy of relaxation at T_g vanishes, leading to thermally reversing glass transitions. The phase diagram permits delineating glass compositions that are in the flexible phase (FP), intermediate phase (IP), and the stressed rigid phase (SRP) for all ternary $Ge_xAs_xS_{100-2x}$ glass compositions. For the IP compositions examined, a general lowering of the molar volumes, V_m, is observed in relation to those for non-IP compositions, giving rise to a volumetric window. Melt dynamics of IP compositions reveal a fragility index, $m < 20$, lower than that for non-IP melts for which $m > 20$ displays a fragility window, underscoring in part the reason for the delayed homogenization of melts in these sulfide glasses. The observations of the three types of window characteristics of IP compositions are feasible only when the homogeneous bulk glasses are synthesized, in which the variance $\langle \Delta x \rangle$ in As and Ge concentrations, x, across batch compositions is less than 0.01%. This is established by Fourier transform–Raman profiling of each batch of composition that is synthesized.

1. Introduction

Topological constraint theory (TCT) provides an atomic-scale description of glass network functionality in terms of network connectivity.[1] Here, network connectivity, $\langle r \rangle$, is taken as the mean coordination number, written as $(\Sigma n_r r)/N$, where n_r represents the number of atoms with the coordination number r, and $N = \Sigma n_r$ represents the total number of atoms of the network. A glass network is viewed as a disordered network of atoms linked by covalent bonds, with the bond lengths between the nearest-neighbor (nn) atoms and bond angles between the second nn atoms to act as mechanical constraints.[1] In an analogy to J. C. Maxwell's ideas on the stability of macroscopic structures,[2] a glass network as a whole is then viewed to be either in a flexible phase (FP) or an isostatically rigid phase or a stressed rigid phase (SRP) if the number of constraints per atom, n_c, is, respectively, lower than, equal to, or higher than the number of degrees of freedom per atom, i.e., three for 3D networks.

The special condition for a network to acquire isostatic rigidity, i.e., $n_c = 3$, stimulated profound interest in the field. Vibrational analysis[1–6] of such networks revealed that the condition $n_c = 3$ is identified with the percolation of rigidity in a glassy network. In its original formulation[1,7] of TCT, the isostatically rigid nature of a network was viewed to occur at a solitary composition. On the other hand, the experiments first showed[8] that such a condition can be realized in laboratory glasses across a wide

---

S. Chakravarty
Department of Mechanical and Materials Engineering
University of Cincinnati
Cincinnati, OH 45221, USA

B. S. Almutairi
Department of Physics
University of Cincinnati
Cincinnati, OH 45221, USA

Dr. R. Chbeir, Dr. S. Chakraborty, Prof. P. Boolchand
Department of Electrical Engineering and Computer Science
University of Cincinnati
Cincinnati, OH 45221, USA
E-mail: boolchp@ucmail.uc.edu

Prof. M. Bauchy
Department of Civil and Environmental Engineering
University of California
Los Angeles, CA 90095, USA

Prof. M. Micoulaut
Laboratoire de Physique Théorique de la Matière Condensée
Sorbonne Université
CNRS
Paris 75252, France

The ORCID identification number(s) for the author(s) of this article can be found under https://doi.org/10.1002/pssb.202000116.

DOI: 10.1002/pssb.202000116

range of chemical compositions, defining an intermediate phase (IP).[8,9] Calorimetric experiments have shown that isostatically rigid networks possess a near-vanishing enthalpy of relaxation ($\Delta H_{\rm nr}$) at T_g, the glass transition temperature, leading to thermally reversing glass transitions and the existence of thermally reversing windows as the signature[10–12] of the IP. As the quality of bulk glass synthesis advanced[13] to obtain homogeneous glasses, the reversibility window (RW) shape changed from being triangular,[14] to Gaussian,[15] to square-well like[11,12] with abrupt edges. The latter experimental finding of a square-well-like RW is fully consistent with theory.[7] Specifically, the onset and end of the RWs define, respectively, the "rigidity" and "stress" elastic phase transitions,[16] in which the controlling parameter is the connectivity, or $\langle r \rangle$ of the network, which is tied to glass compositions. Theory has shown both these percolative phase transitions to be of the first order.[17] In experiments, this requires the variance of the alloying species (A, B, C) in a multicomponent $A_xB_yC_z$ batch composition synthesized to be typically 0.1% or lower.

The inclusion of T-dependent bond-stretching and bond-bending constraints in TCT, analytically,[6,18–20] and then using molecular dynamics (MD) simulations,[21,22] opened a new vista by extending the domain from a strictly $T = 0$ K theory to examining glass structures at finite T. More importantly, it permitted probing the melt[21,22] structure and dynamics and linking these to glass topological phases (TPs).

Experiments have also shown that glass compositions across the IP display remarkable functionalities, including a high liquid-like configurational entropy,[23] which led such networks to 1) display the qualitatively suppressed aging of glass physical properties including the $\Delta H_{\rm nr}$ term,[24,25] 2) form compacted networks[26,27] with reduced molar volumes, 3) form networks that can adapt,[28] 4) form networks that can display high fracture toughness,[29] and 5) form networks that display minimum creep[30–32] among others. These arrays of profound functionalities have stimulated much excitement in theory,[18,33,34] in experiments,[35,36] and in applications[37,38] of these materials. The development of high-K dielectrics in standard 3T devices was made feasible by the recognition of a self-organized interface layer between Si and SiO_x ($x = 1$), on which the high-K dielectric layer is built.[39] The qualitative suppression of aging of IP-built glasses and amorphous materials offers a distinct advantage in using such glasses in any application such as continuum emission in the IR,[40] phase change memory materials,[41] and 3D X-point memory materials[38,42] where sustainability is necessary.

For a glass network composed of atoms with a coordination number, 'r' = 1 or greater; the condition for percolation of rigidity[43] ($n_c = 3$) can be written as follows

$$\langle r \rangle_c = 2.40 - 0.4\ (n_1/N) \tag{1}$$

For glass networks that do not contain dangling ends ($n_1 = 0$), such as group IV (Si, Ge) chalcogenides (S, Se), one recovers the Phillips–Thorpe condition[1,4] for the onset of rigidity near $\langle r \rangle_c = 2.40$ from Equation (1). On the other hand, for group V (P, As) chalcogenides (S, Se), wherein two oxidation states with different local structures can exist, such as a quasitetrahedral (QT) $S = As(S_{1/2})_3$ local structure (As^{5+}) or a pyramidal (PYR) $As(S_{1/2})_3$ local structure, (As^{3+}) one recognizes[44] that although both these local structures are isostatic ($n_c = 3$), their connectivities $\langle r \rangle$ are quite different, with QT units possessing a lower $\langle r \rangle = 2.28$ than PYR units possessing $\langle r \rangle = 2.40$. For these reasons, one expects and indeed observes the IP in binary P–Se[45] and As—Se[44,46] glasses to span approximately the connectivity range $2.28 < \langle r \rangle < 2.40$.

The goal of the present work is directed toward mapping the Global TP diagram of the Ge—As—S ternary glass system over the glass-forming range. The TPs in the Ge—S binary[24] and the As—S binary[47] became available recently, once a dedicated effort to homogenize melts/glasses was made[46,48,49]. The TPs in the equimolar $Ge_xAs_xS_{100-2x}$ ternary are reported[50] here. In combination with the TPs in the Ge—S and As—S binary, we have now constructed a global TP diagram of the Ge—As—S composition triangle. By homogenizing melts/glasses during synthesis in ex situ Raman profiling experiments,[47,50] one could observe the elusive 537 cm^{-1} mode of the S = As stretch of QT $S = As(S_{1/2})_3$ local structure. The homogenization of the present ternary glasses also was made feasible, observing the reversibility, fragility, and volumetric windows each localized in the IP range of compositions. Finally, new simulation results using first-principles molecular dynamics are presented here. These simulation results show that the large atomic motion involved in flexible Ge—As—S melts is associated with profound structural modifications that involve a global modification of S—S correlations and the emergence of metal–metal bonds for compositions belonging in the IP.

The article is organized as follows. In Section 2, we provide details on glass synthesis and homogenization and on the simulation details. The calorimetric and volumetric results on the three materials systems, As—S binary, Ge—S binary system, and the equimolar Ge—As—S, are presented in Section 3. Ab initio melt diffusivities are compared with the experimental fragility index in Section 4. In Section 5, we develop the TP diagram in the Ge—As—S ternary and then compare it with the one in its Se counterpart, Ge—As—Se ternary. The conclusions are summarized in Section 6.

2. Synthesis and Glass/Melt Homogenization

In this section we briefly describe the synthesis and homogenization of binary As_xS_{100-x} and ternary $Ge_xAs_xS_{100-2x}$ glasses. In both these glass systems, once the glasses are homogenized, the direct evidence for the normal modes of the As-centered QT local structure, $S = As(S_{1/2})_3$, is observed in Fourier Transform (FT)–Raman scattering. Although these sulfide glasses have been examined in many previous investigations,[51–63] we are unaware of any previous report on the evidence of the As=S stretch mode at 537 cm^{-1}, as observed recently[47,50] in these glasses. The observation highlights the crucial need to homogenize glasses to observe the three TPs to decode the physics of the glassy state. We provide in Sections 2.1 and 2.2 details on the synthesis and homogenization of, respectively, binary As_xS_{100-x} and equimolar ternary $Ge_xAs_xS_{100-2x}$ melts/glasses.

2.1. Synthesis and Homogenization of Binary As_xS_{100-x} Glasses

Batches of 1.5 grams in the size of 5'9s pure starting materials, S and As_2S_3, from Cerac Inc. in the form of small lumps

(2–4 mm diameter) were sealed in an evacuated (3×10^{-7} Torr) dry quartz tube of 5 mm internal diameter (ID). The starting materials were alloyed at 650 °C for an extended period in a box furnace, keeping the quartz tubes vertical, and it led to a melt column of about 15 mm in length. The vapor pressure of elemental sulfur exceeds 10 atmospheres at $T > 650\,°C$.[64] Periodically, the FT–Raman spectra of the melt column were taken at five locations, and the process of alloying continued till the spectral line shapes became identical when the variance $\langle \Delta x \rangle$ in As content typically reduced from 5% or more to 0.01%, and the melt/glass specimen was then taken to be homogeneous. **Figure 1** shows a typical result for a binary As_xS_{100-x} glass composition at $x = 19\%$. Each glass sample synthesized was subjected to FT–Raman profiling to ascertain its homogeneity before undertaking other types of measurements. A Model 870 FTIR FT–Raman system from Thermo-Nicolet using 1064 nm radiation from a Nd-YAG laser, with a spot size of 50 μm and 125 mW power, was used to excite Raman scattering. In a typical measurement we acquired 200 scans.

Raman spectra of the glasses (Figure 1) are dominated by three features, a broad mode centered near 350 cm^{-1}, resulting from the glass backbone composed of As-centered QT and PYR, narrow features from S_8 rings near 217 and 472 cm^{-1}, and a mode due to S_n polymeric chains near 461 cm^{-1}. After 6 days of alloying (Figure 1), one observes a significant variance in the ratio R of the scattering strength of the S_8 ring modes near 472 cm^{-1} normalized to the backbone mode centered near 350 cm^{-1}. In the early stages, the melt column position 1 close to the top but below the meniscus is S rich, whereas position 5 at the bottom of the melt is As rich. This is the case because the density of As_2S_3 (3.43 g cm^{-3}) exceeds that of pure S (2.0 g cm^{-3}). The gravitationally induced segregation is most helpful in tracking how the homogenization process evolves as As diffuses to the top and S to the bottom of the melt column. Remarkably one can track the heterogeneity by merely examining about 2% of the melt column in five Raman scattering measurements. As the alloying process continued from 6 days to 33 days (Figure 1), the variance in As content (**Figure 2**a) deduced by plotting R as a function of melt position could be converted into As or Ge content x with the aid of an empirical calibration (Figure 2a). We found that the variance in x decreased from 4.88% to nearly 0.28%. At that point we decided to heat the glass to $T = 105\,°C$ for 2 days, permitting the fragmented segments of the glass backbone between the amorphous S_8 ring phase to coalesce and grow. Here we must remember that the $T = 105\,°C$ exceeds T_g of the

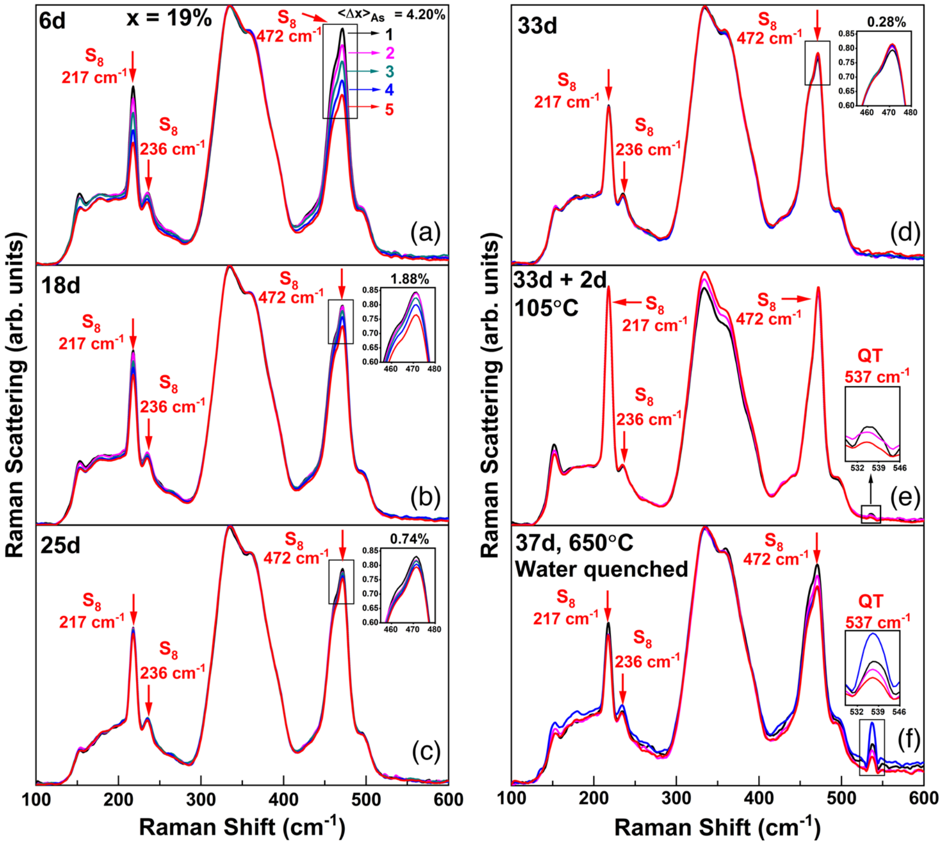

Figure 1. FT–Raman scattering of $As_{19}S_{81}$ glass alloyed a) for $t_r = 6$d, displays an As variance $\langle \Delta x \rangle_{As} = 4.20\%$, b) for $t_r = 18$d, the variance reduced to 1.88%, c) for $t_r = 25$d, reducing further to 0.74%, and d) for $t_r = 33$d, saturating to 0.28%. In each panel the Raman spectra from position 1 (S rich) to position 5 (As rich) has been indicated. The reduced As variance across the 1.5 g batch composition is taken as evidence of glass homogenization upon continued alloying. In (d), the homogenized melt/glass upon thermal quench from 650 °C displays a segregated backbone immersed in a sea of S_8 ring fragments. In (e) heating the glass at $T_g + 10\,°C = 105\,°C$ for 2 d results in fragments of the backbone coalescing and the observation of the 537 cm^{-1} mode of QT units. In (f) by taking the glass of (e) to 650 °C for 2 d and water quenching, it leads to the further growth of the elusive 537 cm^{-1} mode and a substantial amount of additional sulfur alloying in the backbone inferred from the qualitative reduction of the S_8 ring fraction between spectra (e) and (f).

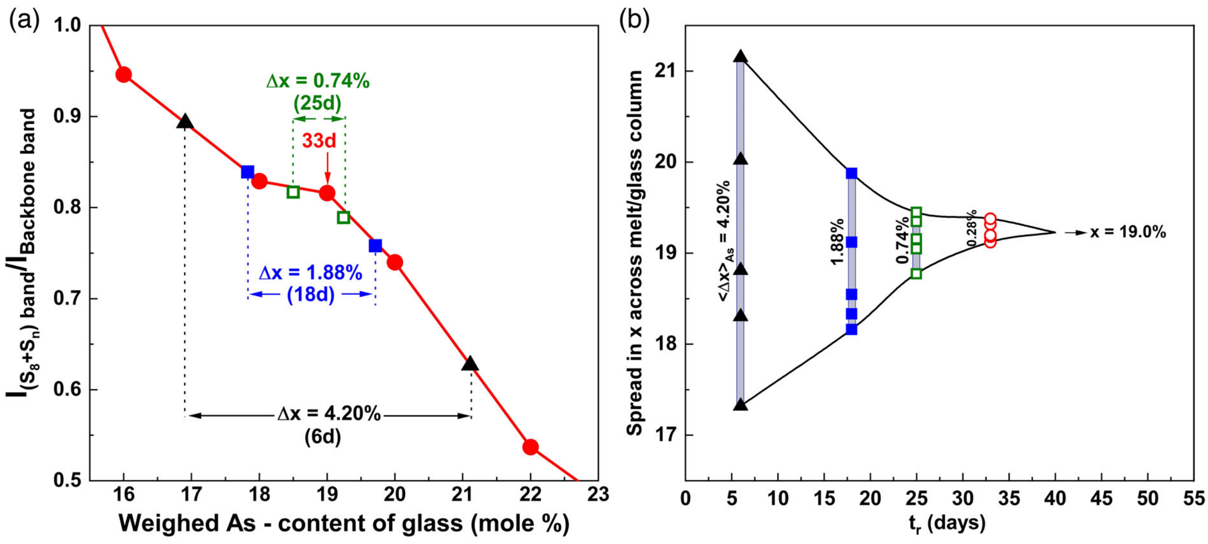

Figure 2. a) The observed variation in the ratio of the scattering strength of the S-related band near 472 cm^{-1} to the backbone band near 350 cm^{-1} plotted against the As content of glasses. The red data points are results obtained on fully homogenized glasses from $x = 16\%$ to $x = 22\%$, with the smooth red curve serving as an empirical curve. Superposed on the calibration plot are the results obtained for a glass sample weighed at $x = 19\%$, as it was alloyed from 6 to 33 d, and the variance $\langle \Delta x \rangle_{\text{As}}$ to decrease from 4.20% to about 0.28%. In (b) the decrease in the As variance, $\langle \Delta x \rangle_{\text{As}}$, is plotted as a function of alloying time, t_r, in days for an $\text{As}_{19}\text{S}_{81}$ glass. It provides a pictorial view of the manner in which the weighed glass at $x = 19\%$ undergoes delayed homogenization.

glass but is lower than 150 °C, the T_λ temperature, when S_8 rings begin to open up into S_n chain segments. One can immediately observe evidence for the mode near 537 cm^{-1} to be manifested by that heat treatment (Figure 1, 35d). The final step was a heat treatment at 650 °C for 2 days, followed by a water quench when the scattering strength of the 537 cm^{-1} mode substantially increased, and the much higher fractions of sulfur as polymeric S_n chains now find themselves in the backbone than that in the S_8 ring phase. A close inspection of the Raman profiles after 35 and 37 d shows a pronounced reduction in the scattering strength of the S_8 ring concentration. The final Raman scattering result after 37 days of alloying is characteristic of the fully homogenized glass, and it shows not only a well-developed mode near 537 cm^{-1} but also the largest fraction of the 350 cm^{-1} broad mode due to the backbone in relation to the S_8 ring scattering. The multistep processing has led to a maximum in the concentration of S to be present in the backbone of the glass as S_n chain configurations.

The plot in the variance of As content as a function of alloying time could be deduced by establishing an empirical calibration (Figure 2a) of the scattering strength ratio R of the S_8 plus S_n contribution to the scattering by the broad backbone mode near 350 cm^{-1} (red curve in Figure 2a), obtained from plotting the results on all the homogenized glass compositions synthesized. By projecting the observed fraction of $S_8 + S_n$ chain to the backbone scattering on this calibration, one could deduce the variance in As content in the melt composition as a whole, $\langle \Delta x \rangle$, as a function of the alloying time. The two orders of magnitude reduction in the As variance across the 1.5-g batch can be seen (Figure 2b) as the melts were alloyed for typically 45–60 days.

Parallel results were obtained in more than a dozen glass compositions in the $\text{As}_x\text{S}_{100-x}$ binary.[47] In general, we found that S-rich glass compositions at $x < 20\%$ took longer to homogenize because of the growth of the amorphous S_8 ring phase, which serves to suppress the formation of the glass backbone as melts are water quenched. Specifically, as melt temperature T is lowered to $T_\lambda = 150\,°\text{C}$, melt regions composed of long S_n chains steadily decouple into more stable S_8 rings from the connective tissue. We next describe the case of the equimolar $\text{Ge}_x\text{As}_x\text{S}_{100-2x}$ ternary,[50] where again we successfully observed the As-based QT local structure in the glasses, but only after bulk glasses were homogenized. These examples serve to highlight the crucial role melt homogenization plays in elucidating the physics and chemistry of these sulfide glasses.

2.2. Synthesis and Homogenization of Ternary $\text{Ge}_x\text{As}_x\text{S}_{100-x}$ Glasses

Bulk glasses of the equimolar $\text{Ge}_x\text{As}_x\text{S}_{100-2x}$ composition were synthesized using 5'9s elemental S platelets, As_2S_3 pieces from Cerac Inc., and elemental Ge pieces in evacuated quartz tubes of 5 mm ID. The batch size was kept at 1.5 g and alloyed at 650 °C for the extended alloying periods of up to 60 days typically while profiling[50] the melt column and wetting the evacuated quartz tube by FT–Raman scattering as illustrated earlier for $\text{As}_x\text{S}_{100-x}$ glasses.[47] In **Figure 3**, we provide the results for a glass composition at $x = 11\%$. In the early stages, $10\,\text{d} < t_r < 52\,\text{d}$, melts steadily homogenize as the S content across the melt column nearly equalizes as t_R increased in the $10\,\text{d} < t_R < 59\,\text{d}$. Remarkably, as the melt/glass homogenizes, the unmistakable evidence of the 537 cm^{-1} mode of the S = As stretch in the QT the $\text{S} = \text{As}(\text{S}_{1/2})_3$ local structure was manifested.

To convert the variance in the scattering strength of the pair of Raman active modes due to S_8 and S_n into the variance of As or

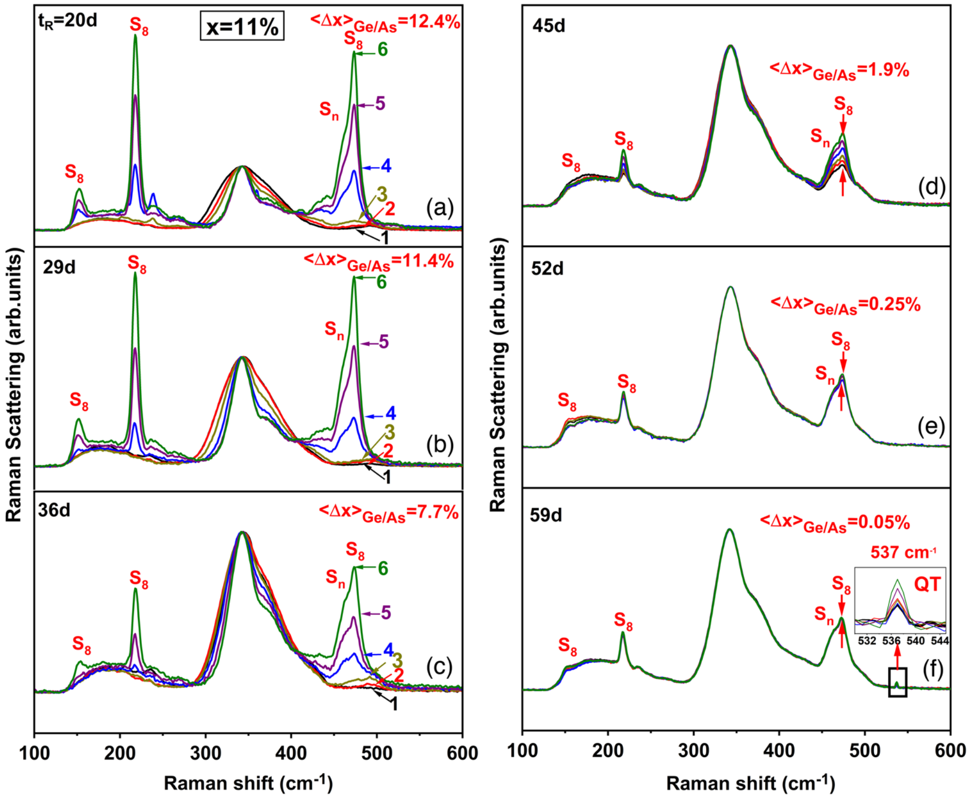

Figure 3. FT–Raman spectra of a $Ge_{11}As_{11}S_{78}$ glass composition after alloying at 650 °C and recorded at six spots along the melt column in percentage. In the panels (a)–(d), the Raman spectra of position 1 represents the As-/Ge-rich region of the melt and position 6 represents the S-rich region. Spectra in (a) and (b) show how the initial chemical reaction takes place. In (c) the bulk glass is formed but it is heterogeneous. In (d), (e), and (f) the bulk glass homogenizes, and the elusive 537 cm^{-1} mode is manifested.

Ge of the glass backbone, we generated an empirical calibration in the ratio R of the Raman scattering strength of the sum of S_n and S_8 mode scattering strengths to the glass backbone mode at 350 cm^{-1} scattering strength for all the homogenized glass compositions, as shown in **Figure** 4a. The sharp decrease in $R(x)$ at low x in the $2\% < x < 7\%$ range, followed by a monotonic decrease in $R(x)$ with increasing x, reflects broadly the pronounced decoupling of S_8 rings from the glass backbone in the S-rich glasses. By projecting R for the five locations along the melt column studied, we could translate the glass heterogeneity in terms of the variance in $\langle \Delta x \rangle$, as shown in Figure 4b. Note that after 59 days, the variance in x decreases by two orders of magnitude. We would like to emphasize that the FT–Raman profiling experiments probe the homogenization of a batch as a whole during synthesis and not a small part of the batch after glass synthesis in Raman or energy-dispersive X-ray measurement. During synthesis, as the stoichiometry of a certain segment of the batch changes, these changes intimately influence the stoichiometry of the rest of the batch globally.

2.3. Molecular Dynamic Simulations

To study the effect of As and Ge modifying atoms into the base sulfur network, we performed a series of first-principles molecular dynamics simulations[65] on identical $Ge_xAs_xS_{100-2x}$ systems containing $N = 249$ atoms at ten different compositions (5%, 8%, 9%, 10%, 12%, 14%, 17%, 18%, 21%, and 25%) with the number of As, Ge, and S atoms fulfilling the desired stoichiometry, ranging over compositional domains where the network is S deficient or where metal–metal bonds will proliferate. A periodically repeated cubic cell was used, whose size changes according to the number density of the glasses. We used density functional theory (DFT) in combination with plane-wave basis sets. The electronic scheme has been chosen after a series of methodological investigations on different liquid chalcogenide glasses and liquids including Ge–X ($X =$ S, Se) and As—Se.[66–68] It should be mentioned that the DFT simulation of Ge—S glasses led to structure functions (structure factor, pair correlation function) that were in excellent agreement with the experimental counterpart.[24] Simulations have also shown that a generalized gradient approximation (GGA) for the exchange-correlation energy improves substantially the description of both the short and intermediate-range order as compared with the local density approximation (LDA).[69] In addition, it was demonstrated that the exchange-correlation functional reducing the metallic character of the bonding (a Becke, Lee, Yang, and Parr [BLYP] functional) led to systems with a reduced number of miscoordinated atoms and metallic character[68] and improved the reproduction of structure functions obtained from neutron diffusion in the liquid and amorphous state.[70–72]

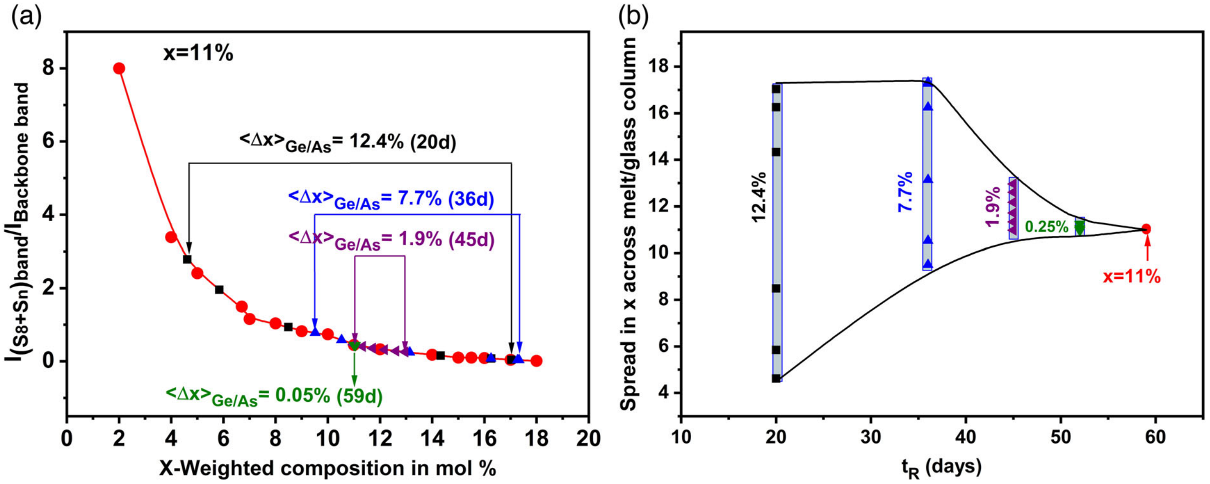

Figure 4. Panel (a) shows the variation in the scattering strength ratio of the S band near 473 cm^{-1} to the backbone band near 342 cm^{-1} on a set of fully homogenized glasses (•) in the range $1\% < x < 19\%$, defining a red empirical curve. The results obtained for a glass composition at $x = 11\%$ are then projected on the calibration curve. The variance in Ge or As concentration, $\langle \Delta x \rangle_{\text{As or Ge}}$, systematically decreases from 12.4% to 0.05% with increasing t_R. In panel (b), the observed variance $\langle \Delta x \rangle_{\text{As or Ge}}$ is plotted as a function of alloying time (t_R), and it shows the manner in which the delayed homogenization of weighted glass at $x = 11\%$ occurs.

Using these recipes, the electronic structure of the As—Ge—S liquids and glasses was described within DFT and evolved self-consistently during the motion, using a GGA for the exchange and correlational parts of the total energy, according to Becke (B) and LYP, respectively.[73,74] Valence electrons were treated explicitly, in conjunction with norm-conserving pseudopotentials to account for core–valence interactions. The wave functions were expanded at the γ-point of the supercell and the energy cut-off was set at 20 Ry. Starting configurations were taken from the corresponding ternary Ge—As—Se glasses,[72] and to reach the desired compositions, either the simulation box was rescaled to match the desired density or As/Ge atoms were randomly replaced by sulfur atoms to meet the desired stoichiometry, prior to box rescaling. Loss of the memory of the initial configurations was achieved through preliminary runs at 1800 K over 50 ps. For all investigated compositions and temperatures (1200 and 800 K), statistical averages in the liquid state were obtained over 20–25 ps of trajectory with a time step of $\Delta t = 0.12$ fs and a fictitious mass of 1000 a.u. To obtain the glassy compositions, we performed quenches from equilibrated trajectories at 800 K and relaxed the systems at 300 K over 30 ps. The resulting structures contain a variety of motifs, ranging from a chain-like sulfur-rich structure (**Figure** 5a,b) to a largely cross-linked network structure containing a large number of metal–metal bonds (Figure 5c). Later, we provide a first account of such simulation results and the whole structural and dynamic properties will be discussed separately.[75]

3. Experimental Section: Calorimetric and Volumetric Properties of As_xS_{100-x}, Ge_xS_{100-2x}, and $Ge_xAs_xS_{100-2x}$ Glass Systems

3.1. Methods

3.1.1. Glass T_g and Enthalpy of Relaxation at T_g

Modulated differential scanning calorimetry (DSC) permitted us to establish the scan rate independent $T_g(x)$, $\Delta H_{nr}(x)$, and specific heat change $\Delta C_p(x)$ of the sulfide glasses using a Q2000 MDSC. The typical operating conditions used included a scan rate of 3 °C min^{-1}, a modulation time period of 100 s, and a modulation amplitude temperature of 1 °C. Scans were initiated from

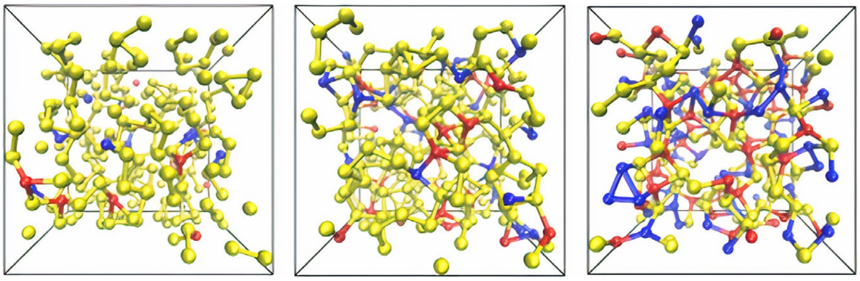

Figure 5. Atomic configurations obtained by FPMD melt-quenched $Ge_xAs_xS_{100-2x}$ melts with (left panel) $x = 5\%$; (center panel) $x = 10\%$; and (right panel) $x = 25\%$. Sulfur, germanium, and arsenic atoms are shown in yellow, red, and blue, respectively. Note the presence of homopolar bonds for the $x = 25\%$ composition.

$T_g - 50\,°C$ to $T_g + 50\,°C$ in a heating mode, followed by a cooling cycle, and the total heat flow deconvoluted in terms of the reversing and nonreversing heat flow terms.[76] From the nonreversing heat flow, we established the modulation frequency corrected $\Delta H_{nr}(x)$ term and from the reversing heat flow the scan rate independent T_g and $\Delta C_p(x)$.

3.1.2. Melt Dynamics through a Measurement of Melt Fragility Index

To establish the fragility index $m(x)$ of melts, scans were initiated from $T_g + 50\,°C$ to $T_g - 50\,°C$ in the cool-down mode and the glass transition exotherm recorded as a complex C_p as a function of modulation frequency. The in-phase C_p shows a step similar to the reversing heat flow, whereas the out-of-phase component of C_p shows a Gaussian profile. The peak of the Gaussian profile corresponds[76,77] to the condition that the enthalpy of relaxation completely tracks the modulated temperature profile, i.e., $\omega\,\tau = 1$. Here, ω represents the modulation frequency and τ the enthalpy relaxation time. As ω is increased, τ decreases as the glass must relax faster to track the impressed modulation frequency. By establishing this, the variation in $\tau(T)$ as a function of temperature, one establishes[76,77] the fragility index $m(x)$.

3.1.3. Molar Volumes and Volumetric Windows

The glass molar volumes were established using the Archimedes principle, using a digital balance with a quartz fiber. Bulk glass samples of 125 mg in weight or larger were weighed in air and then in 200 proof ethyl alcohol to achieve an accuracy of 0.5% or less in the density measurements. A Ge single-crystal standard was used to calibrate the density of alcohol. As an overall check on the accuracy of the density measurements, we measured the density of a pure Si wafer. Molar volumes were then extracted using the measured densities.

3.2. Material Systems

3.2.1. Binary As_xS_{100-x} Melts/Glasses

We established the scan rate independent, $T_g(x)$, the glass transition temperature, $\Delta H_{nr}(x)$, and specific heat change, $\Delta C_p(x)$, of the sulfide glasses using a Q2000 MDSC. The typical operating conditions used a scan rate of $3\,°C\,min^{-1}$, a modulation time period of 100 s, and a modulation amplitude temperature of 1 °C. Scan were initiated from $T_g - 50\,°C$ to $T_g + 50\,°C$ in a heating mode, followed by a cooling cycle, and the total heat flow deconvoluted in terms of the reversing and nonreversing heat flow terms. From the nonreversing heat flow, we established the modulation frequency corrected $\Delta H_{nr}(x)$ term and from the reversing heat flow the scan rate independent T_g and $\Delta C_p(x)$.

To establish the fragility index of melts, scans were initiated from $T_g + 50\,°C$ to $T_g - 50\,°C$ in the cool-down mode and the glass transition exotherm was recorded as a complex C_p as a function of modulation frequency. The in-phase C_p shows a step similar to the reversing heat flow, whereas the out-of-phase component of C_p showed a Gaussian profile.

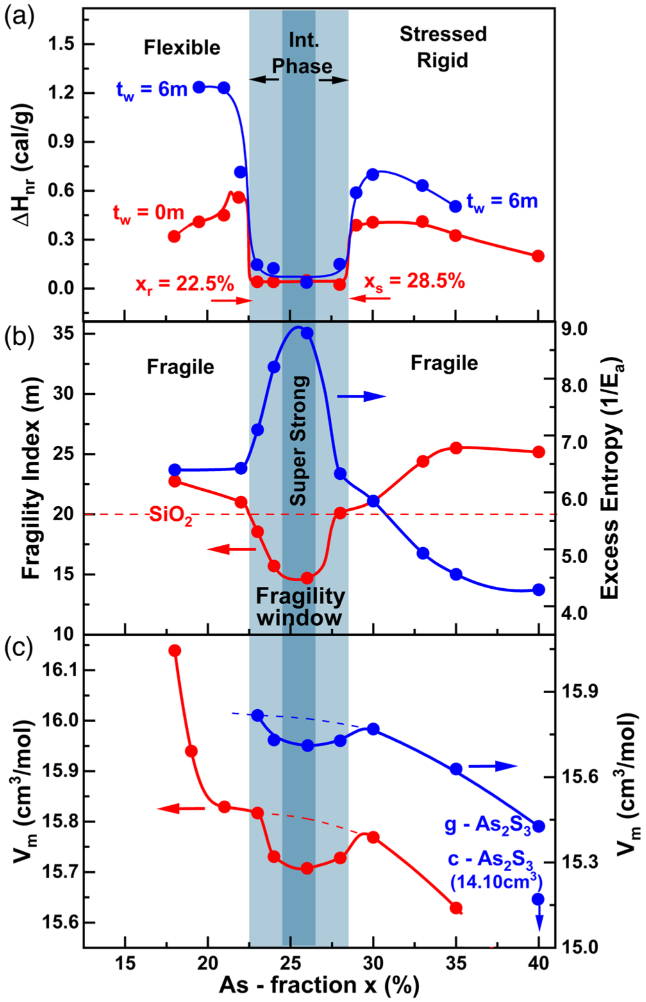

Figure 6. Compositional trends of As_xS_{100-x} glasses (data taken from Figure 13 of Chakravarty et al.[47]) in a) enthalpy of relaxation at T_g (ΔH_{nr}), b) melt fragility index, and c) glass molar volumes displaying local minima in the $22.5\% < x < 28.5\%$ range, the light blue panel. In (b) we also plot the inverse of the activation energy, E_a, for enthalpy relaxation times. In (a) the light blue panel gives the glass RW, in (b) compositions for which $m < 20$ defines the fragility window, and in (c) the local minimum in molar volumes illustrates the volumetric window in glasses. To better illustrate $V_m(x)$ results at $x > 30\%$, we have redrawn the data on a coarser ordinate scale on the right to illustrate the reduction in V_m in both g- and c-As_2S_3 (14.10(2) cm^3).[78]

The enthalpy of relaxation at T_g, $\Delta H_{nr}(x)$, and the fragility index $m(x)$ in binary As_xS_{100-x} glasses[47] are shown in **Figure** 6a,b, respectively. Molar volumes of the glasses were established using the Archimedes principle and a digital balance, a quartz fiber, 200 Proof alcohol, and the liquid weighing medium were used. Bulk glass specimen of about 125 mg in weight or more was used to establish the molar volume to obtain an accuracy of 0.5% or less, and the results are shown in Figure 6c.

One of the first reports on measuring $\Delta H_{nr}(x)$ in As—S glasses by MDSC was by Wagner et al. in 1998. It is remarkable that some of their findings on calorimetric data are in good agreement with the present ones.[47] Trends in $\Delta H_{nr}(x)$ in rejuvenated glasses ($t_w = 0$ m) displayed a square-well-shaped RW (Figure 6a), with the onset near $x_r = 22.5\%$, or $\langle r \rangle = 2 + x = 2.22$, defining the rigidity transition and the end point near $x = x_s = 28.5\%$, or $\langle r \rangle = 2.28$ represents the stress transition. Upon room temperature aging of glasses for $t_r = 6$ m, note that the $\Delta H_{nr}(x)$ term nearly quadrupled in the FP and nearly doubled in the SRP but remained unchanged in the IP. Trends in the fragility index, $m(x)$, displayed a Gaussian-like minimum for IP range compositions, whereas the configurational entropy that varies as the inverse of the E_a displayed a maximum in the IP range. The qualitatively suppressed aging in the IP range of compositions was in harmony with the high configurational entropy of these melt compositions.

The glass molar volumes showed a local minimum that was fully localized in the IP range of glass compositions. In an earlier work,[53] where a deliberate effort to homogenize batches by FT–Raman profiling was not conducted, one found the volumetric window to be smeared at the edges of the window, underscoring that $V_m(x)$ results did indeed carried vital information on network packing.

3.2.2. Binary Ge_xS_{100-x} Melts/Glasses

The calorimetric and volumetric results on especially homogenized binary Ge_xS_{100-x} were first reported in 2014[24] and are shown here (**Figure 7**) for completeness, as we correlated these findings with ones on corresponding sulfides in the binary As—S and ternary $Ge_xAs_xS_{100-2x}$ glasses.[47,50] In the Ge_xS_{100-x} binary, the enthalpy of relaxation, $\Delta H_{nr}(x)$, displayed a square-well-like RW, in the $19.3\% < x < 24.9\%$ range. The rigidity transition at the onset of the RW corresponded to $\langle r \rangle = 2(1 + x) = 2.39$, whereas the stress-elastic phase transition at the end of the RW corresponded to $\langle r \rangle = 2.49$. Thus, we note that the IP in Ge_xS_{100-x} glasses was significantly upshifted in $\langle r \rangle$ in relation to the IP in binary As_xS_{100-x} glasses (see the previous section).

Trends in the fragility index (Figure 7b), $m(x)$, displayed a minimum for IP melt compositions, with $m < 20$ and with $m > 20$ for non-IP melt compositions, thus displaying a fragility window. Unlike the case of the As—S binary, where the window was Gaussian like and symmetric about the centroid composition of the IP, the fragility widow in the Ge_xS_{100-x} binary was found to be asymmetric, with the global minimum in m occurring near $x = 25\%$ of Ge toward the upper edge of the IP. The asymmetric fragility window in the Ge_xS_{100-x} binary was not an accident, it was tied to the presence of a small and finite concentration of S_8 ring fraction for IP glasses that monotonically decreased in the $20\% < x < 24\%$ range as x increased, as revealed in Raman scattering measurements.[24] The presence of these S_8 rings that was decoupled from the backbone clearly contributed to an increased fragility of melts. But remarkably it did not influence the enthalpy of relaxation of the glasses in the IP. This was a remarkable feature of the IP in the glasses, which apparently adapted to the isostatic nature of the glasses ($n_c = 3$), as manifested in the vanishing $\Delta H_{nr}(x)$. This feature of self-adaption was also observed in the equimolar $Ge_xAs_xS_{100-2x}$, as we comment later.

Trends in molar volumes of the glasses as a function of composition (Figure 7c) displayed a minimum centered about the IP composition (light-grey panel). The minimum was asymmetric about the center IP composition, which we understand because of the increasing presence of S_8 rings as x decreases in the $25\% > x > 20\%$ range. The same structural feature, viz., presence of the S_8 rings, contributed to the asymmetry of the fragility window.

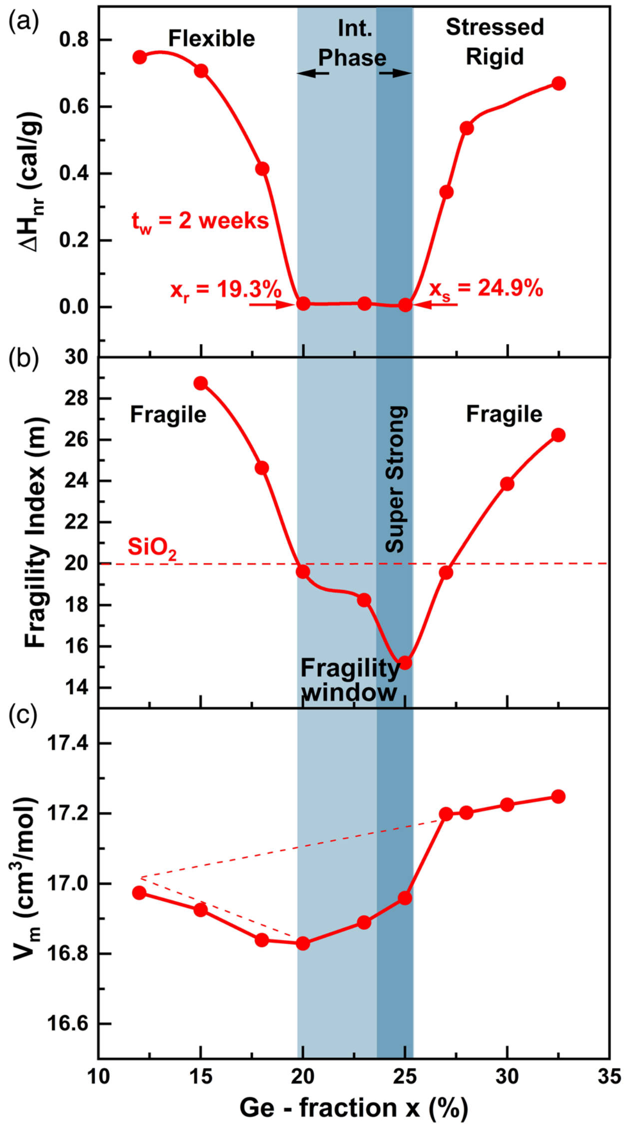

Figure 7. Compositional trends of a) enthalpy of relaxation at T_g (ΔH_{nr}), b) melt fragility index, and c) glass molar volumes in Ge_xS_{100-x} glasses. The figure is based on data from Figure 8–10 of Chakraborty et al.[24] The RW in (a) resides in the $19.3\% < x < 24.9\%$ range, the light blue panel coincides with the fragility window in (b) where $m < 20$ in the window and $m > 20$ outside the window. Molar volumes, $V_m(x)$, display a global minimum in the light grey panel defining the volumetric window. The dark grey panel gives the super-strong melt compositions where $m = 15$, the lowest value.

3.2.3. Ternary $Ge_xAs_xS_{100-2x}$ Melts/Glasses

The observation of the RW in the present ternary[50] (**Figure 8a**) fixed the three TPs. Glass compositions at $x < 9.0\%$ or $\langle r \rangle < 2.27$

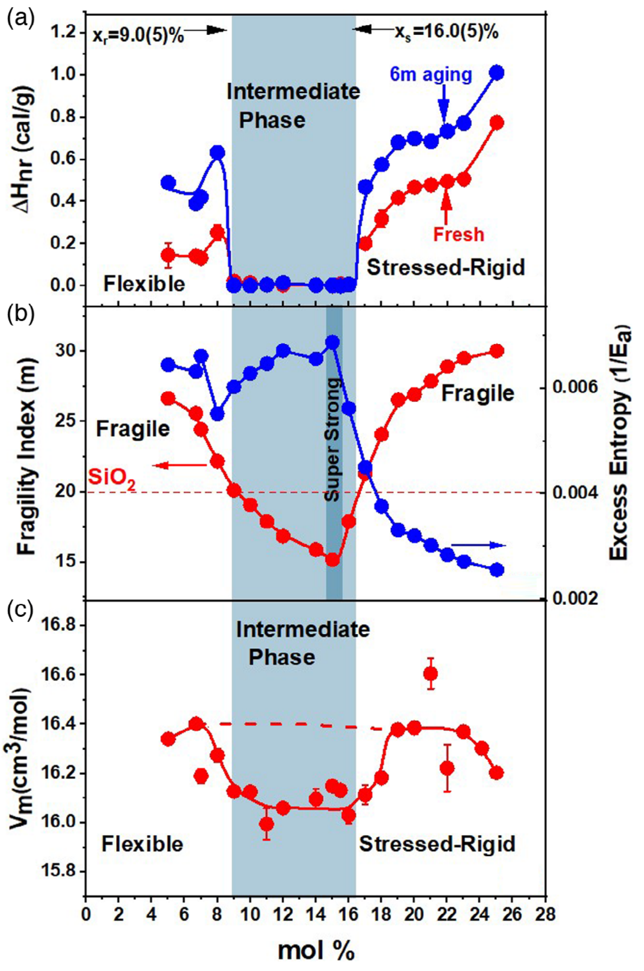

Figure 8. Compositional trends in a) enthalpy of relaxation ΔH_{nr} at T_g in the range $9\% \leq x \leq 16\%$, b) melt fragility index (m) and excess entropy ($1/E_a$), and c) molar volumes for homogenized $Ge_xAs_xS_{100-2x}$ ternary glasses.[50] In (a) the glass RW (blue panel) gives rise to strong melts with $m < 20$ (b) which displays the fragility window. In (c) trends in Molar volumes show a minimum in the IP composition range, defining a volumetric window.

were in the FP, those at $x > 16.0\%$ or $\langle r \rangle > 2.48$ were in the SRP, whereas those at $9.0\% < x < 16.0\%$ or $2.27 < \langle r \rangle < 2.48$ were in the IP. The enthalpy of relaxation, ΔH_{nr}, measured after 6 months of room temperature aging of the glasses in the hermetically sealed Al pans used in the fresh state (0 months) revealed a doubling of the enthalpic term in the FP and the SRP, but the term remained unchanged in the IP.

The fragility index $m(x)$ variation with melt composition[50] (Figure 8b) revealed a minimum, with $m < 20$, for IP compositions, but increased steadily with $m > 20$ both in the flexible and stressed rigid compositions. The asymmetric nature of the fragility window with $m = 15.0$ near $x = 15\%$ was tied to finite but the steadily decreasing concentration of S_8 rings in the $9\% < x < 15\%$, as revealed by the Raman scattering measurements. A parallel feature was noted in the Ge_xS_{100-x} glasses (previous section).

The fragility index measurements (Figure 8b) also yielded the activation energy for enthalpy relaxation, E_a. Following Adams and Gibbs,[79] one can show that the inverse of E_a yielded a measure of the configurational entropy S_c. The super-strong character of a melt in the IP, understandably, then gave rise to a broad increase in S_c in that phase. For these reasons, one expected IP glasses to possess a high configuration entropy and on general thermodynamic considerations to display qualitatively suppressed aging, as we noted from Figure 8a.

It is most curious that the increase of molar volumes $V_m(x)$ (Figure 8c) at the phase boundaries where the rigidity and stress transitions are manifested also represent compositions were the enthalpy of relaxation, $\Delta H_{nr}(x)$ shows an abrupt increase defining the walls of the RW. The square-well-like variation in $V_m(x)$ (Figure 8c) noted in the present ternary glasses[50] was observed in several earlier reports,[58,80,81] although the connection of network packed to the existence of the IP was not recognized. On general considerations, one expected the enthalpy of a system to be related to its internal (U) and molar volumes (V) and pressure (P) by Equation (2)

$$H = U + PV \tag{2}$$

There was an abrupt increase in the volume of a glass at the edges of the IP where the two elastic phase transitions occur. Equation (2) shows that the enthalpy H of a glass system generically also increases. In the calorimetric measurements the jump in the nonreversing heat flow, $\Delta H_{nr}(x)$, was thus fully consistent with (2). At glass compositions further into the FP away from the rigidity transition, other features of the structure were manifested that could either decrease (or increase) the nonreversing enthalpy of relaxation by lowering (or increasing) the entropy of a glass system as it aged. For example, in selenides, as one gets into the FP and as the length of polymeric Se_n chains increases, there is clear evidence for these flexible chains correlating and thereby lowering the entropy of the glass structure, a feature that leads to the $\Delta H_{nr}(x)$ term to increase.[82] In the $Ge_xAs_xS_{100-2x}$ ternary sulfides,[50] on the other hand, as one starts from the rigidity transition and moves into the FP, the S_8 ring phase grows with an attendant loss of glass backbone that is reflected in a reduction of ΔH_{nr} (Figure 8a).

4. Numerical Results from Structural Models

Prior to structural analysis, it must be stated that the small simulation box and the short simulation time do not permit detecting S_8 rings in sulfur-rich compositions (see, e.g., Figure 5a). The T_λ transition temperature below which such rings segregate from the backbone is found, indeed, at a low temperature (e.g., at 393 K in the analogous sulfide As_5S_{95}[83]), and the timescale for such ring nucleation has been found to be well beyond computer timescale capabilities, including from classical MD using dedicated force fields and stimulated annealing procedures.[84] **Figure 9** shows the obtained partial pair correlation functions for different compositions in the Ge—As—S glasses at 300 K. It can first be noticed that the obtained heteropolar bond distances involving Ge and As (Ge—S and As—S) are in very good agreement with experimental work and with reverse Monte Carlo (RMC) fitted structure models. Both partials (Figure 9b,c) display a strong peak at $r = 2.25$ Å in g_{Ge-S} and g_{As-S} that serve as the

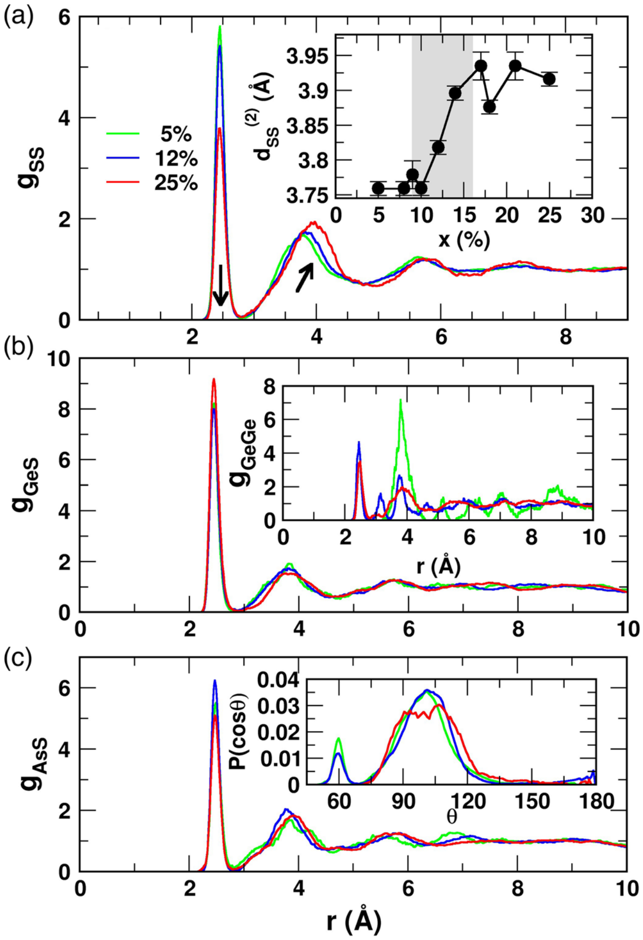

Figure 9. Partial pair correlation functions from FPMD simulations in Ge–As–S glasses for selected compositions (5%: green, 12%: blue, 25%: red): a) g_{S-S}, b) g_{Ge-S}, c) g_{As-S}, and inset of (b) shows g_{Ge-Ge}. The inset in (a) shows the secondary correlating distance $d_{S-S}^{(2)}$ as a function of Ge/As content x. The inset of (c) represents the S–S–S BAD (a cutoff of 2.9 Å has been used). Arrows in (a) indicate the evolution of the peaks.

definition of the tetrahedral and PYR geometrical motifs. The strong peaks furthermore suggest that in such As- and Ge-deficient compositions, the network is dominated by essentially heteropolar bonding. The calculated bond distances ($d_{As-S} = d_{Ge-S} = 2.46$ Å for $Ge_{25}As_{25}S_{50}$) are somewhat higher than those determined from the work of Soyer-Uzun et al.,[85] who found from RMC and also from a combination of neutron and X-ray diffraction[86] a distance of 2.25 Å for the main peak, similar to those obtained for the corresponding binaries Ge–S[87] (2.21 Å). Conversely, the homopolar distances of Ge–Ge (2.47 Å, inset of Figure 9b) and As–As (2.49 Å for $Ge_{21}As_{21}S_{52}$) which appear at large compositions are found to be in agreement with the results determined from the similar experimental methods (2.46–2.48 Å for the average Ge/As–Ge/As bond distance[86,85]).

With increasing As/Ge content, the amplitude of the S–S pair correlation function decreases (Figure 9a), in contrast with the behavior of the one in As–S and Ge–S correlations (Figure 9b,c). Interestingly, it is found that the second neighbor correlating distance found at, e.g., $d_{SS}^{(2)} = 3.75$ Å for sulfur-rich compositions shifts to larger distances with increasing Ge/As content (3.92 Å for $x = 25\%$). Once this evolution is tracked with modifier content, one notices that the growth of such distances occurs across the IP so that the FP is characterized by a small $d_{S-S}^{(2)}$ distance. An inspection of the atomic configurations indicates that such a modification is driven by the reduction of the probability of finding S chain fragments and the emergence of the network bonding sulfur between As or Ge geometrical motifs (S–Ge/As–S) that furthermore gives rise to rings of even sizes containing a homopolar S–S bond. As a result, the corresponding bond distance is still present in the partial S–S pair correlation function at the largest composition (25%, Figure 9a). A corresponding S–S–S bond angle distribution (BAD) (inset of Figure 9c) has been calculated and indicates a global reduction of the typical angle found in elementary sulfur (106°), and a broadening of the distribution under the increasing network stress is found for the largest composition (25%). A selection of BAD is, furthermore, discussed later.

With increasing composition, the emergence of metal–metal bonds (As–As, Ge–Ge, and Ge–As) is obtained and these

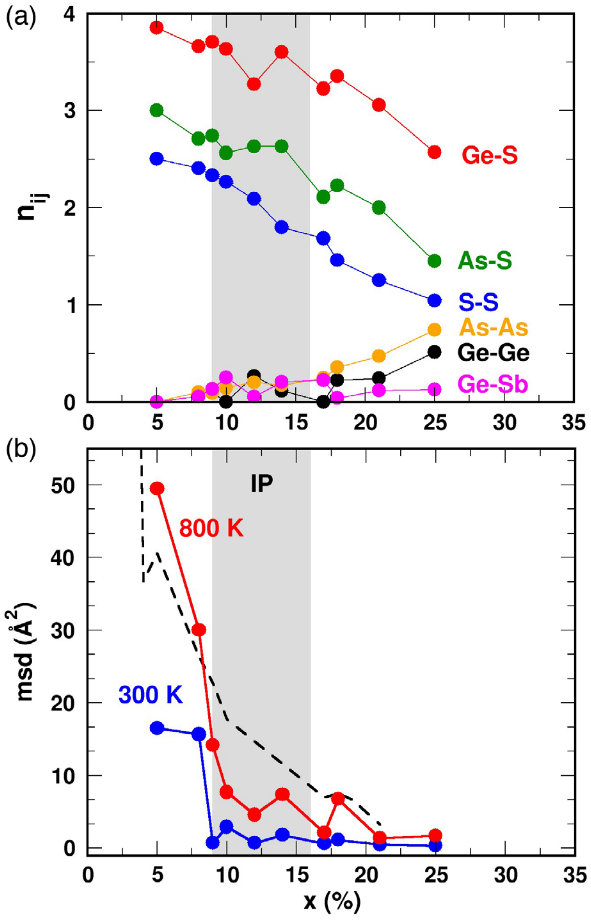

Figure 10. a) Calculated partial coordination numbers n_{ij} as a function of the modifier content. The gray zone indicates the IP. b) Calculated sulfur MSD after 20 ps simulation at 800 K (red) and 300 K (blue) as a function of Ge/As content. The broken line represents the same quantity in Ge–As–Se melts at 900 K.[49]

increase substantially in the IP (**Figure 10**a), consistently with previous findings in As—Se[88] or Ge—Se glasses,[71] albeit debated for the latter from the recent isotopic-substituted neutron diffraction.[89] Here, it is detected that the formation of As—As bonds is favored with respect to Ge—Ge bonds, whereas the mixed metal–metal As—Ge remains at a rather small level. Taken together, one finds that the coordination number of As, Ge, and S is 3, 4, and 2, respectively, and, for e.g., the $x = 14\%$ composition, one obtains $n_{\mathrm{As}} = n_{\mathrm{AsS}} + n_{\mathrm{AsAs}} + n_{\mathrm{AsGe}} = 3.01$. We furthermore note that for the largest composition, there is an increased tendency to form several As-rich motifs in the simulation box (blue structures in Figure 5c) and these might represent some elementary fragments of the Realgar phase that manifests by nanoscale phase separation (NSPS) in the corresponding glasses. Raman scattering of the stoichiometric $\mathrm{As_2S_3}$ glass synthesized by quenching melts at $T_{\mathrm{q}} > 350\,°\mathrm{C}$ reveals a steadily increasing fraction of Realgar units decoupling[47,90] from the glass backbone as T_{q} increases.

Figure 10b now shows some dynamic features. The calculation of the mean square displacement (MSD) $\langle r^2(t)\rangle$ of the three species (As, Ge, and S) leads to a usual profile on a log–log plot representing $\langle r^2(t)\rangle$ with time, i.e., a ballistic regime in a short time where the behavior scales as t^2. However, we notice that for the considered temperatures (800 K and, of course, 300 K), the diffusive regime does not set in within 20–30 ps, and instead a sluggish cage-like dynamics is obtained (not shown) that does not follow the typical behavior, $\langle r^2(t)\rangle = t$. We, therefore, focus on the evolution of an averaged MSD after 20 ps with a composition that can provide some hints on the special relaxation and glassy dynamics behavior observed experimentally. An inspection of the behavior with the composition clearly indicates that the MSD results contain features of the underlying TPs. The MSD is, indeed, found to be very small at large Ge/As content (MSD = 6 Å^2 for $x = 10\%$ at 800 K) and in stressed rigid glasses, with the extent of motion being almost identical between the 800 K melt and the 300 K glass (2 Å^2), which corresponds to a distance that is less than interatomic distances. This suggests a frozen motion due to the large cross-link density. As the sulfur content increases, IP compositions seem to lead to a slight increase in $\langle r^2(t)\rangle$, barely visible from the figure, and the most noticeable change is obtained at the intermediate-to-flexible boundary, $\langle r^2(t)\rangle$ starting to dramatically increase to reach nearly 50 Å^2 for $x = 5\%$ at 800 K. The same trend is observed to a lesser extent at 300 K, and for compositions belonging to the FP the MSD is about 16 Å^2. These results actually parallel those found in corresponding ternary selenides (broken curve in Figure 10b), and here it was also found that flexible Se-rich glasses display an enhanced motion in the liquid state.[49]

5. Discussion

5.1. Construction of the Global TP Diagram of Ternary Ge—As—S glasses

The availability of RWs for the three sulfide glass systems (**Figure 11**) of interest in the present work opens the possibility of examining their broad consequences. Foremost, these RWs fix the three TPs in the respective sulfides, as shown in Figure 11, with glass compositions at a lower (higher) $\langle r\rangle$ than the IP range representing the flexible (stressed rigid) elastic phases. The IP width in the As—S binary (Figure 11a), labeled as "A," extends in the range $2.22 < \langle r\rangle < 2.285$ of the mean coordination number,[47] whereas the IP in the Ge—S binary[24] of width, labeled as "B," extends in the mean coordination range, $2.386 < \langle r\rangle < 2.50$ (Figure 11b).

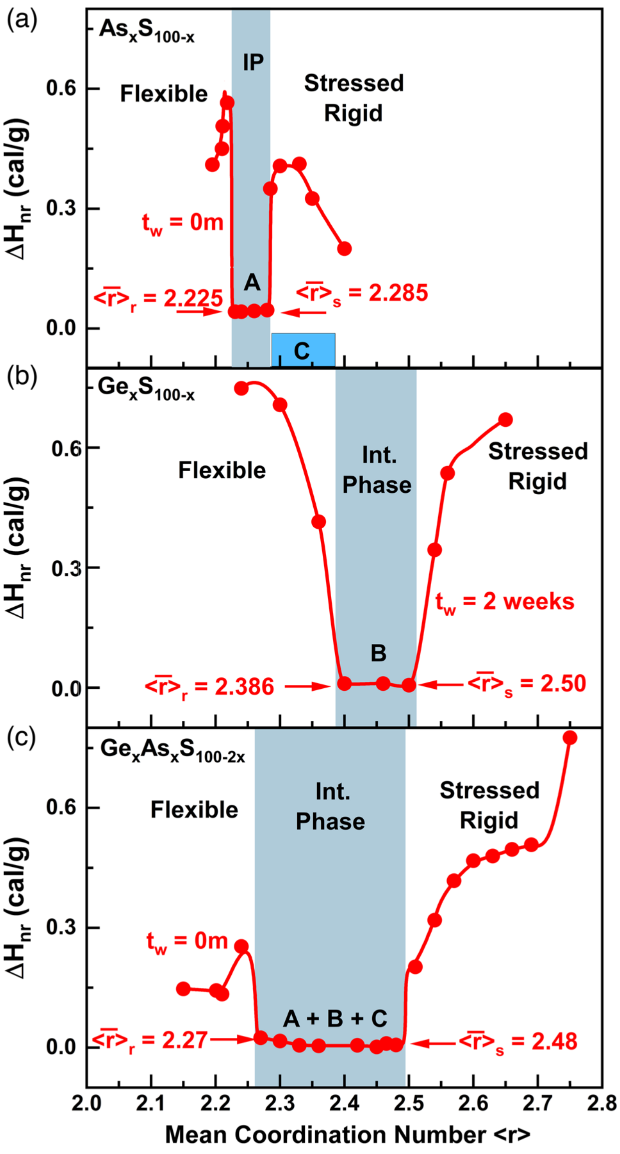

Figure 11. RWs a) for Ge$_x$S$_{100-x}$ glasses of width A, b) for As$_x$S$_{100-x}$ glasses of width B, and c) for Ge$_x$As$_x$S$_{100-2x}$ glasses of width A + B + C as a function of $\langle r\rangle$, the mean coordination number. From As—S to the Ge—As—S, the width of the RW approximately increases in $\langle r\rangle$ by an amount $C = 0.10$, essentially the blue bar between the observed RWs between Figure 8a and b. The RW width in Ge—S of B is retained in the Ge—As—S ternary. These features are shown in Figure 7.

The IP of the Ge—S binary of width B appears to be common to that of the Ge—As—S ternary. Furthermore, the IP in the Ge—As—S ternary[50] of width, labeled as "A + B + C" (Figure 11c), extends in the mean coordination range,

$2.27 < \langle r \rangle < 2.48$, and it can be viewed to be a superposition of the IPs in the respective binary systems (A + B) plus something additional (C). Specifically, in comparing the IPs in the As—S to the Ge—As—S, the width of the RW approximately increases in $\langle r \rangle$ by an amount C or $\langle r \rangle = 0.10$, essentially the gap between the windows in Figure 11a,b shown as the shaded blue bar. We clarify the structural origin of the width C and some of its consequences.

We have projected the IP observed in the three sulfide glass systems onto the Ge—As—S composition triangle in **Figure 12.** Both Figure 11 and 12 assist in understanding some broad features of glass structures prevailing in the IP of the Ge—As—S ternary glass systems.

The IP (Figure 12) is made of the following three segments; a segment A colored green, a segment B colored indigo, and then a segment labeled C colored blue. The equimolar glass compositions shown as the brown line passing through the red filled circles bisect the segment C into an "upper part" and a "lower part." The "upper part" is derived from the contribution to network self-organization due to steadily alloying Ge in As—S glasses and must be made up of contributions of local structures such as corner sharing (CS) and edge sharing (ES) GeS_2 tetrahedra with $\langle r \rangle = 2.40$, and this is manifested in the experiments as the blue bar labeled C in Figure 11a. On the other hand, the "lower part" of segment C comes from the contribution of alloying As in Ge—S glasses, and it must derive from the presence of QT $S{=}As(S_{1/2})_3$ local structures formed in the glasses with $\langle r \rangle = 2.28$, along with the prevailing Ge-centered CS and ES tetrahedra. For a similar chalcogenide (As_2Se_3), we have recently reported evidence[91] that the population of QT, albeit rather small[88] (5%), leads to a specific spectroscopic infrared (IR) signature at 370 cm^{-1}, in agreement with experimental findings. The numerical study indicates that these defect geometries are largely dependent on thermal history, are reminiscent of the high-temperature liquid where fourfold As represents the dominant structural motif, and they relax to the PYR As structure under certain numerical preparation conditions. In the present ternary, evidence from FPMD is obtained for such motifs at low compositions, as discussed later.

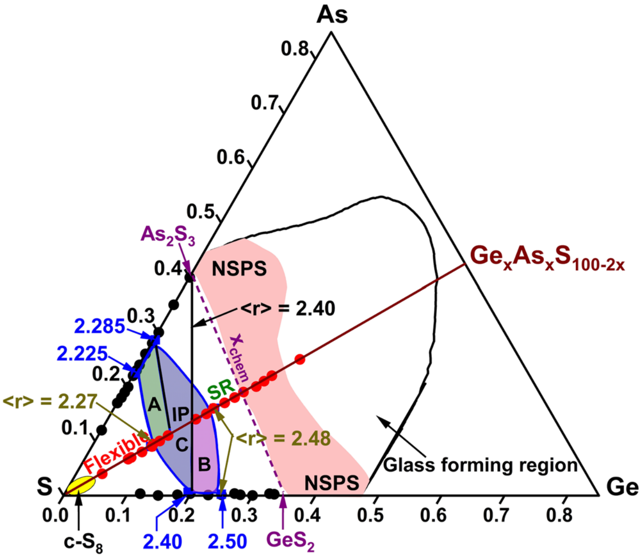

Figure 12. TPs observed in As_xS_{100-x} binary, Ge_xS_{100-x} binary, and $Ge_xAs_xS_{100-2x}$ ternary are projected on the Ge—As—S compositional triangle. Starting from pure S, as we move along the S—As we have the IP of width A (green) in the As_xS_{100-x} binary. Along the S—Ge binary, we have the IP of width B (indigo) in the Ge_xS_{100-x} binary. For the equimolar compositions, one spans the FP $(0 < \langle r \rangle < 2.27)$ and the IP $(2.27 < \langle r \rangle < 2.48)$ followed by the SRP (>2.48), with the red data points showing the glass compositions examined in the ternary $Ge_xAs_xS_{100-2x}$ system. The IP of the equimolar is made up of three parts A + C + B. Part A is approximately the IP of As_xS_{100-x} binary (green), whereas part B is the IP of the Ge_xS_{100-x} binary (indigo). See text for details on the C region (blue).

A perusal of the Ge—As—S composition triangle also shows that the FP is formed toward the S vertex of the triangle. The structure of these S-rich compositions is composed of two types of networks, one consisting of an amorphous S_8 ring-rich phase and a connective tissue composed of bulk $Ge_xAs_yS_z$ glass in which Ge and As content are quite low, $x < 0.20$, $y < 0.20$. The amorphous S_8 ring-rich phase serves as an impediment in the synthesis of homogeneous binary and ternary glasses.[47,50] Close to the vertex at the S point, melts essentially reveal crystalline sulfur composed of the rhombic phase[92] (colored yellow) in Figure 12.

Glass compositions with mean $\langle r \rangle > 2.50$, exceeding the IP range, exist in the SRP, as labeled in Figure 12. And as glass network compositions exceed the chemical threshold ones, which is delineated by the broken black line joining As_2S_3 with GeS_2, glasses broadly feature NSPS as depicted by the light brown region. In As_xS_{100-x} binary glasses, the glass-forming tendency rapidly disappears[90,93] once $x > 40\%$, as As_4S_4 monomers rapidly form, resulting in a loss of connective tissue defining the glass backbone, and for that reason, understandably, no glass formation is observed once $x > 44\%$. Along the equimolar $Ge_xAs_xS_{100-2x}$ ternary glass compositions, experiments show[50] that the formation of As_4S_4 and As_4S_3 monomers occurs as $x > 18.18\%$, contributing to a mild NSPS of the glasses. Some of the excess Ge, at $x > 18.18\%$, takes on a distorted octahedral coordination as in amorphous GeS, as revealed from Raman scattering.[50] Nevertheless, the glass-forming tendency continues because a substantial part of As and Ge persists as part of the connective tissue at $x > 18.18\%$, defining the glass backbone. The NSPS feature of stressed rigid ternary Ge—As—S glasses was also recognized in an earlier study.[94] Along the Ge_xS_{100-x} binary, at $x > 33.3\%$, there is substantial evidence from Raman scattering and ^{119}Sn Mossbauer spectroscopy where the tetrahedrally coordinated local structure prevailing near the chemical threshold (GeS_2) steadily transforms into the ethane-like Ge_2S_3 local structure possessing Ge—Ge bonds and distorted Rocksalt-type GeS local structures[95] in which Ge takes a quasi-sixfold coordination with three short and three long bonds. Thus, glass compositions in the NSPS regime will not conform to the 8N bonding rule. To use the global Ge—As—S composition triangle as a means to obtain glasses of different connectivities by merely using the 8N bonding rule would clearly be inappropriate for the regimes where NSPS occurs.

5.2. Adaptation of S_8 Rings in the IP of Ge—S and Ge—As—S Glass Systems

The special nature of the network self-organization in the IP of the chalcogenides was recognized quite early in the field of glass science.[28] The absence of network stress,[96] resulting from the absence of redundant bonds in the IP of binary Ge_xSe_{100-x} glasses, was taken as evidence for such glassy networks to have the functionality of adaptability. In the present work, Raman scattering results on Ge_xS_{100-x} binary and $Ge_xAs_xS_{100-2x}$ ternary[47,50] show that there is a finite concentration of S_8 rings that persists in the IP of these glasses. The results for the Ge_xS_{100-x} binary show that the S_8 concentration monotonically decreases in the $20\% < x < 25\%$ and vanishes near $x = 26\%$ (**Figure 13**). An examination of the glass enthalpy of relaxation reveals a square-well-like RW (Figure 7a). On the other hand, melt fragility index variation with a composition reveals a global minimum near $x = 25\%$, the same composition at which the S_8 content nearly vanishes. Due to the presence of S_8 rings in the melt, one expects the fragility index of melts to increase as the S_8 monomeric species would form nonbonding interactions with the glass network. It stands to reason that as the S_8 ring content increases from 25% to 20% (Figure 13c), the melt fragility index would increase (Figure 13b). Most remarkable is the fact that the enthalpy of relaxation at T_g for the IP glasses remains minuscule across the IP (Figure 13a). The observation clearly suggests that the presence of a small but finite concentration of a nonbonding S_8 species apparently does not influence the isostatic nature of the glassy state (Figure 13a). On the other hand, the melt fragility index variation with composition reveals a global minimum near $x = 25\%$, the same composition at which the S_8 content nearly vanishes.

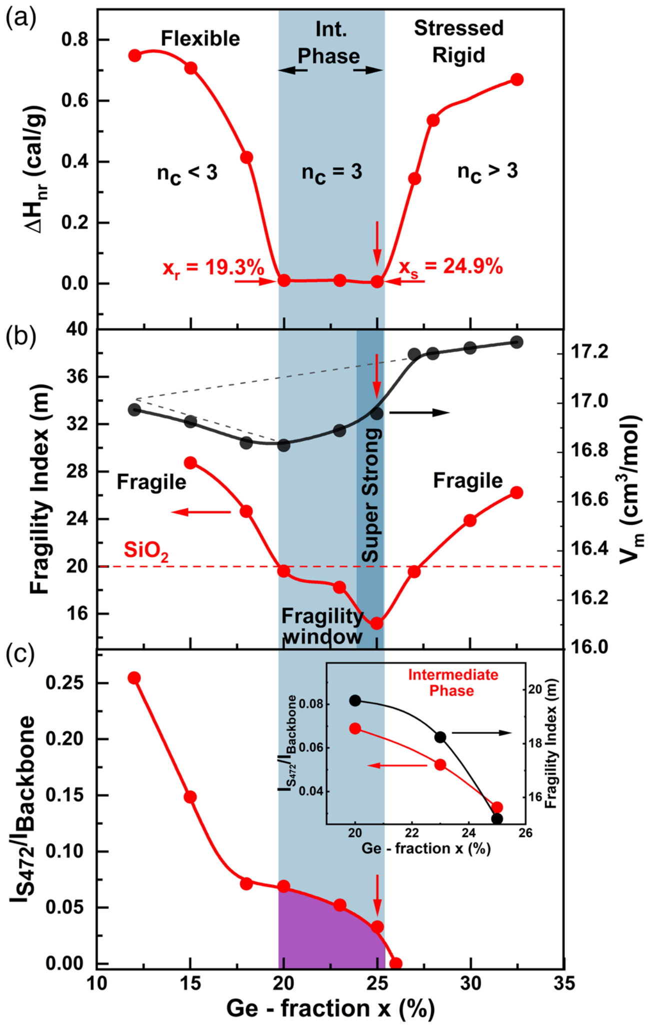

Figure 13. Scattering strength ratio of the S_8 ring mode near 472 cm^{-1} normalized to the backbone scattering strength near 340 cm^{-1} plotted as a function of Ge content x of glasses. Note that the S_8 concentration remains finite in the IP but steadily decreases to vanish near $x = 26\%$.

Parallel results are obtained on the equimolar $Ge_xAs_xS_{100-2x}$ ternary,[50] wherein Raman scattering shows a monotonically decreasing content of S_8 rings to coexist with the glass backbone in the IP glass compositions. For example, at $x = 9\%$, one finds that the S_8 content as measured by the fraction of the scattering strength from 472 cm^{-1} to the broad 340 cm^{-1} mode is found to be about 15%. The S_8 ring fraction steadily decreases with increasing x and vanishes near $x = 15\%$.[50] In such glasses, we find the enthalpy of relaxation at T_g to be vanishing for all IP compositions, leading to a square-well-like variation of the RW (Figure 8a). On the other hand, we find the fragility index $m(x)$ of the melts to increase in proportion to the S_8 ring fraction in the composition range $9\% < x < 15\%$ (Figure 8b). The superstrong melt composition is then manifested near $x = 15.0\%$, where $m = 15.0$. These findings underscore that the self-organized IP in these sulfide glasses will adapt to retain their isostatic character even with a finite content of a foreign nonbonding species like S_8 monomers.

5.3. Functionality of QT $S = As(S_{1/2})_3$ Local Structures and Onset of Rigidity in Group V Chalcogenides

The P_xSe_{100-x} binary glass system is an illustrative example of a group V chalcogenide wherein an IP is observed[45] in harmony with the known local structures. In this binary there are two isostatically rigid ($n_c = 3$) local structures including QT $Se = P(Se_{1/2})_3$ and PYR $P(Se_{1/2})_3$ local structures well documented in Raman scattering[45] and ^{31}P NMR.[97] The connectivity $\langle r \rangle$ of the QT and PYR local structures is respectively 2.28 and 2.40. In **Figure 14**c, we see the IP[45] onsets near $\langle r \rangle = 2.28$ and ends near $\langle r \rangle = 2.40$, in harmony with our expectation that the IP is composed of these two types of isostatically rigid ($n_c = 3$) local structures.

The RWs in the As_xS_{100-x} binary[47] and the $Ge_xAs_xS_{100-2x}$ ternary[50] along with the compositional trends in the scattering strength of the 537 cm^{-1} mode, which is signature of the As=S stretch vibration of QT $S = As(S_{1/2})_3$ local structures, are shown in Figure 14a,b, respectively. The group V sulfide glasses differ from the ground V selenides in one important way. In elemental S and S-rich glasses, S_8 rings are more stable than polymeric S_n chains. The reverse circumstance prevails for the case of pure Se and Se-rich glasses, wherein the polymeric Se_n chains are the more stable structural entity than Se_8 rings. The S_8 rings form part of an amorphous S_8 ring phase in the S-rich ($\langle r \rangle < 2.18$) glasses. This particular phase is not only the predominant structural species but functionally its presence inhibits the growth of the glass backbone by the usual melt-quench route unless the multistep processing of these S-rich glasses is followed, as described recently.[47] The challenge to observing 537 cm^{-1} in

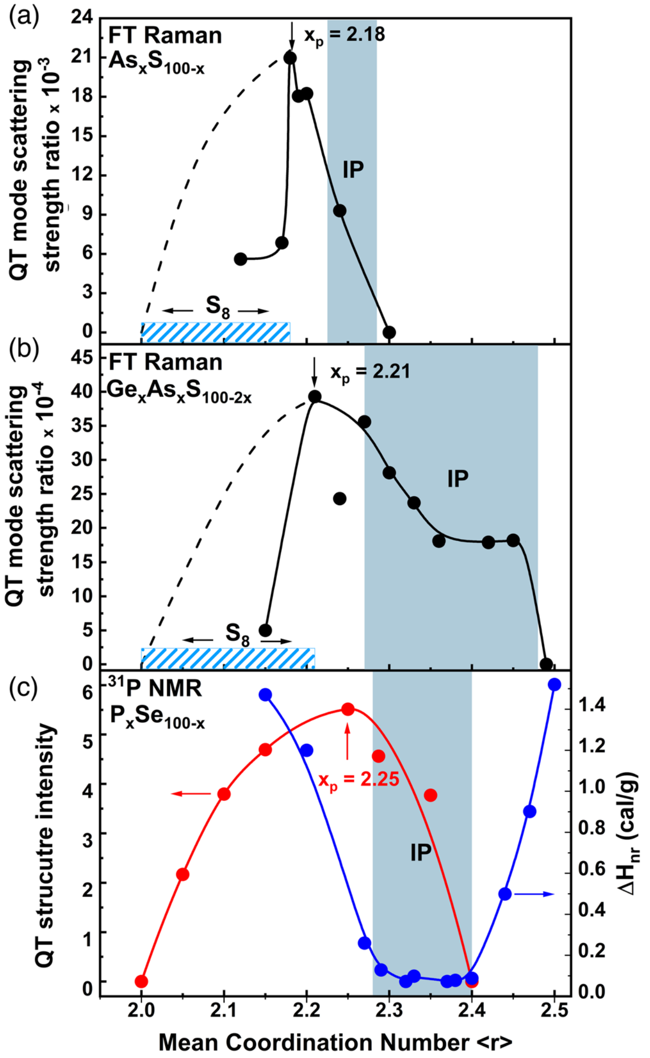

Figure 14. Compositional trends in a) the normalized Raman scattering strength of 537 cm^{-1} of the QT (S = As(S$_{1/2}$)$_3$) local structures observed in As_xS_{100-x} glasses, b) the normalized Raman scattering strength of 537 cm^{-1} of the QT (S = As(S$_{1/2}$)$_3$) local structures observed in $Ge_xAs_xS_{100-2x}$ glasses,[50] and c) ^{31}P NMR signal of QT (Se = P(Se$_{1/2}$)$_3$) local structures in binary P–Se glasses. In (c) we also show the observed IP that extends in the $2.28 < \langle r \rangle < 2.40$ range from the study by Georgiev et al.[45] Note that the maxima in the scattering strength of the QT mode in each panel indicated by arrows are compositions that are precursive to the onset of rigidity. The broken black line in (a) and (b) represents the expected variation in the scattering strength of the QT local structure in the S-rich glasses ($\langle r \rangle < 2.18$), had there been no S_8 ring-based amorphous phase (light blue hashed region). Also note in each case studied, (a)–(c), the QT local structure is observed across the IPs.

these S-rich glasses is tied to the homogeneity of the glasses and then growth in the size of the backbone so that more of the sulfur in a chain configuration can be alloyed in the backbone.

The overall variations in the scattering strength of the 537 cm^{-1} mode of the QT local structures normalized to that of the glass backbone as a function of $\langle r \rangle$ in the As—S binary (Figure 14a) and the Ge—As—S ternary[50] (Figure 14b) display

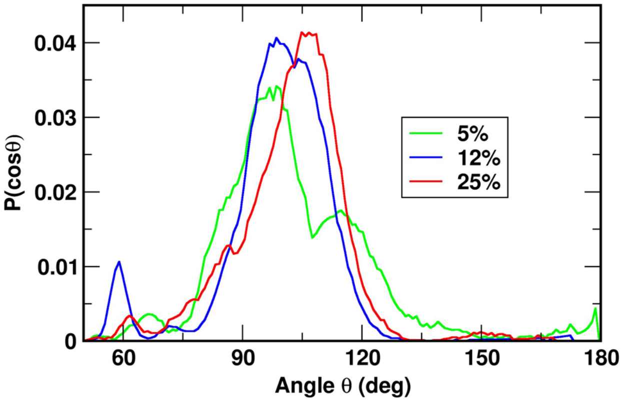

Figure 15. Calculated S—As—S BAD in $Ge_xAs_xS_{100-2x}$ glasses (300 K): $x = 5\%$ (green), 12% (blue) and 25% (red).

features that are qualitatively similar to the one observed in the P–Se binary glasses. Note that in each case the QT local structure scattering strength (concentration) shows a maximum slightly below the IP composition range. In the P–Se binary, one can clearly track the concentration of these species all the way down to pure Se. But such is not the case with the two sulfides glasses for reasons discussed earlier. The synthesis of S-rich glasses requires that these glass batches be fully homogenized and suitably heat treated at a super T_g temperature to promote the growth of the glass backbone. This exercise is vital to elucidate the TPs and the structure manifestations of these phases. A fingerprint to the existence of QT units is provided by the calculated S—As—S BAD from the FPMD structure models (**Figure 15**). Here it is found that for the lowest composition (5%), the S—As—S BAD is bimodal in character with a component at 98° corresponding to the dominant PYR geometry.

The onset of rigidity in these group V chalcogenides is apparently controlled by the QT local structures and understandably onsets near the stoichiometry of the local structure ($\langle r \rangle = 2.28$). The onset of the stress transition in such glasses is then determined by the PYR local structure (As(S$_{1/2}$)$_3$). The structure evidence for the PYR local structure in the family of group V chalcogenides abounds. Experiments[45,97] show that the concentration of these PYR units displays a maximum near $\langle r \rangle = 2.40$, corresponding to the connectivity of these local structures. For these reasons, one expects, and indeed observes, the IP to be broadly located in the $2.28 < \langle r \rangle < 2.40$ range (Figure 14c).

5.4. Comparing the Global TP Diagram of Ternary Ge—As—S Glasses with Ge—As—Se Counterpart

The global TP diagram of the Ge—As—Se composition triangle was recently reported.[49] It is of interest to examine how the present results on the global TP diagram of the Ge—As—S, the corresponding sulfide glasses differ from those of the selenides. To facilitate the comparison, we show the two global TP diagrams adjacent to each other in **Figure 16**a,b. There are striking similarities between the two TP diagrams but also glaring differences.

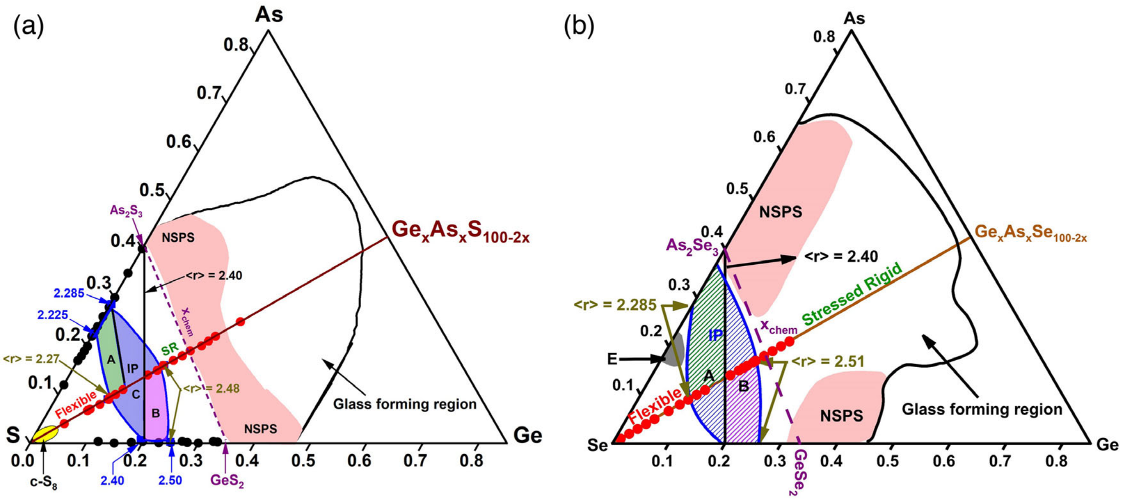

Figure 16. Glass-forming regions in the Ge_xAs_x(S or Se)$_{100-2x}$ taken from Borisova.[98] a) The composition triangle of $Ge_xAs_xS_{100-2x}$ shows the IP in As_xS_{100-x} binary (A, green),[47] Ge_xS_{100-x} binary (B, indigo),[24] and the equimolar $Ge_xAs_xS_{100-2x}$ (A + B + C, blue).[50] b) The composition triangle of $Ge_xAs_xSe_{100-2x}$ shows the IP in As—Se (A, hashed green),[44] in Ge—Se (B, hashed indigo),[13] and in the equimolar (A + B) $Ge_xAs_xSe_{100-2x}$[49] ternary. The FP is localized closer to the S or Se corner, and the SRP between the IP and the chemical threshold composition is delineated by the broken line joining As_2(Se or S)$_3$ with Ge(Se or S)$_2$.

The width of the IP along the equimolar $Ge_xAs_xSe_{100-2x}$ glass compositions spans the range $2.28 < \langle r \rangle < 2.51$, which is nearly the same as in the corresponding sulfide glasses of $2.27 < \langle r \rangle < 2.48$. The width of the IP in the Ge_xSe_{100-x} binary of $2.40 < \langle r \rangle < 2.51$ is nearly the same, as in the corresponding sulfide glasses of $2.40 < \langle r \rangle < 2.50$. In As_xSe_{100-x}, the IP width spans the range $2.28 < \langle r \rangle < 2.37$, whereas in the As_xS_{100-x} binary, the IP spans not only a shorter width of $2.225 < \langle r \rangle < 2.286$, but it is shifted to a lower value of $\langle r \rangle$. The shift to a lower $\langle r \rangle$ is related to some fraction of polymeric S_n chains in As_xS_{100-x} bulk glasses that are decoupled from the backbone, as discussed in a previous study.[47] For these reasons one does not see the IP width A in the As_xS_{100-x} binary glasses and the width B in Ge_xS_{100-x} binary glasses to add up exactly to the IP width in the equimolar $Ge_xAs_xS_{100-2x}$ ternary.[50] On the other hand, in the Ge—As—Se ternary glasses (Figure 16b), one observes the IP width A in the As—Se binary, and IP width B in Ge—Se binary glasses exactly equals the IP width A + B observed in the equimolar $Ge_xAs_xSe_{100-2x}$ ternary glasses.

Some of the glaring differences in the global TP diagram between the Ge—As—S glasses and Ge—As—Se are as follows. There is clear evidence of a mild NSPS along the equimolar $Ge_xAs_xS_{100-2x}$ glasses as x exceeds the chemical threshold, $x_c = 18.18\%$ (Figure 15a); there is no evidence of such NSPS in the Ge—As—Se ternary glasses for the equimolar compositions (Figure 16b). A perusal of Figure 16 shows that the domain of the IP is greater in the Ge—As—Se ternary (Figure 16b) than that in Ge—As—S (Figure 16a). A consequence of the previous observation is that in the Ge—As—S ternary there is a fairly large domain of stressed rigid glass compositions in the sulfide glasses in relation to the selenide glasses. It has been suggested from statistical mechanics calculations that the intermediate phase may be the result of a competition between entropy and enthalpy of melts/glasses.[99]

6. Conclusions

We provide direct evidence for a square-well-like RW in specially homogenized equimolar $Ge_xAs_xS_{100-2x}$ ternary glasses,[50] which has permitted fixing the three TPs. Parallel observations were recently reported on the As_xS_{100-x} binary[47] and Ge_xS_{100-x} binary[24] and these permitted fixing the TPs in the two binary glass systems. By combining results on the two binaries with the one on the ternary glass system, we have now constructed here, for the first time, the global TP diagram for the Ge—As—S composition triangle. The regions of where the three TPs are manifested are identified. The regions where NSPS in the SRP occurs are highlighted. In the specially homogenized melts/glasses, we succeeded in observing for IP compositions besides the 1) RW a 2) a Gaussian-like minimum in the melt fragility index, $m < 20$, defining a fragility window, 3) a Gaussian-like minimum in molar volumes, defining a volumetric window, and finally 4) for the As—S binary and the Ge—As—S ternary, unambiguous evidence for the 537 cm^{-1} Raman active mode of As=S stretch of the As-centered local structure of QT $S = As(S_{1/2})_3$ units. The delayed homogenization of these As- and Ge-based sulfide glasses after over 30–60 days of alloying is due to 1) the super-strong character of the IP melts, 2) the high vapor pressure of elemental sulfur, requiring starting materials to be alloyed at $T < 650$ C, and 3) the formation of an S_8 ring-based amorphous S phase formed in the S-rich glasses that hinder the growth of the glass network backbone. First-principles MD simulations permit producing structural models that are compatible with experimental findings from neutron and X-ray diffraction, while also independently suggesting that the FP has a much larger atomic motion due to the weak bond density of the melts. There are weak effects from structural changes and first-neighbor Ge—S and As—S distances remain constant as they define the elementary tetrahedral and PYR geometries.

However, an obvious increase in the second-correlation S—S distance across the IP is acknowledged, and such distances substantially increase between 10% and 18%. For the case of the Ge_xS_{100-x} binary and the $Ge_xAs_xS_{100-2x}$ ternary, Raman scattering results show clear evidence of a steadily decreasing concentration of S_8 rings across the IP from the rigidity transition composition to the edge of the stress phase transition composition. In spite of such segregation, the enthalpy of relaxation at T_g for glasses vanishes across the width of the IP, underscoring that the isostatic nature of glasses in the IP remains intact. On the other hand, melt fragility index m steadily decreases from 20 to about 15 for the IP glass composition as the S_8 ring content vanishes. These findings highlight the self-adaptation functionality of the isostatically rigid networks formed in the IP as the finite concentration of a nonbonding structural species (such as S_8 rings) proliferates in the networks.[100] In summary, the exceptional functionalities of IP compositions displaying an RW, a fragility window, a volumetric window, and the feature of network self-adaption have been observed in the present sulfide glasses. The qualitative suppression of aging of IP-built glasses and amorphous materials offers a distinct advantage in using them in any application where material sustainability is paramount, such as continuum emission in the IR[40] and phase change memory.[41]

Acknowledgements

P.B. acknowledges support from NSF grant DMR 08-53957. M.M. acknowledges the support of Agence Nationale de la Recherche (ANR), grant no. ANR-11-BS08-10012, from American Fulbright Commission and International Materials Institute (H. Jain). M.B. acknowledges support from NSF, grant nos. 1562066 and 1928538. B.A. was supported by Princess Nourah Bint Abdul Rahman University, Riyadh, Saudi Arabia.

Conflict of Interest

The authors declare no conflict of interest.

Keywords

configurational entropy, fragility indices, melt dynamics, modulated differential scanning calorimetry, Raman scattering, topological phases

Received: February 29, 2020
Revised: April 18, 2020
Published online: May 10, 2020

---

[1] J. C. Phillips, *J. Non-Cryst. Solids* **1979**, *34*, 153.
[2] J. C. Maxwell, *Philos. Mag. (Ser. 4)* **1864**, *27*, 294.
[3] M. F. Thorpe, *J. Non-Cryst. Solids* **1983**, *57*, 355.
[4] J. C. Phillips, *J. Non-Cryst. Solids* **1981**, *43*, 37.
[5] J. C. Phillips, *Solid State Commun.* **1983**, *47*, 203.
[6] J. C. Mauro, *Am. Ceram. Soc. Bull.* **2011**, *90*, 31.
[7] M. F. Thorpe, *J. Non-Cryst. Solids* **1985**, *76*, 109.
[8] D. Selvanathan, W. J. Bresser, P. Boolchand, B. Goodman, *Solid State Commun.* **1999**, *111*, 619.
[9] a) P. Boolchand, D. G. Georgiev, B. Goodman, *Adv. Mater.* **2001**, *3*, 703; b) M. Micoulaut, *Phys. Rev. B* **2006**, *74*, 184208.
[10] M. Micoulaut, *J. Phys.: Condens. Matter* **2010**, *22*, 285101.
[11] S. Bhosle, K. Gunasekera, P. Boolchand, M. Micoulaut, *Int. J. Appl. Glass Sci.* **2012**, *3*, 189.
[12] S. Bhosle, K. Gunasekera, P. Boolchand, M. Micoulaut, *Int. J. Appl. Glass Sci.* **2012**, *3*, 205.
[13] S. Bhosle, K. Gunasekera, P. Chen, P. Boolchand, M. Micoulaut, C. Massobrio, *Solid State Commun.* **2011**, *151*, 1851.
[14] X. Feng, W. J. Bresser, P. Boolchand, *Phys. Rev. Lett.* **1997**, *78*, 4422.
[15] P. Boolchand, P. Chen, D. I. Novita, and B. Goodman, in *Rigidity and Boolchand intermediate phases in nanomaterials* (Eds: M. Micoulaut, M. Popescu), Optoelectronic Materials and Devices, Vol. *6*, INOE, Bucharest **2009**, pp. 1–36.
[16] M. F. Thorpe, D. J. Jacobs, M. V. Chubynsky, J. C. Phillips, *J. Non-Cryst. Solids* **2000**, *266–269*, 859.
[17] D. J. Jacobs, M. F. Thorpe, *Phys. Rev. Lett.* **1995**, *75*, 4051.
[18] P. K. Gupta, J. C. Mauro, *J. Chem. Phys.* **2009**, *130*, 094503.
[19] J. C. Mauro, *Curr. Opin. Solid State Mater. Sci.* **2018**, *22*, 58.
[20] J. C. Mauro, A. Tandia, K. D. Vargheese, Y. Z. Mauro, M. M. Smedskjaer, *Chem. Mater.* **2016**, *28*, 4267.
[21] M. Bauchy, M. Micoulaut, *J. Non-Cryst. Solids* **2011**, *357*, 2530.
[22] M. Bauchy, M. Micoulaut, M. Celino, S. Le Roux, M. Boero, C. Massobrio, *Phys. Rev. B* **2011**, *84*, 054201.
[23] L. Yan, *Nat. Commun.* **2018**, *9*, 1359.
[24] S. Chakraborty, P. Boolchand, *J. Phys. Chem. B* **2014**, *118*, 2249.
[25] S. Chakravarty, D. G. Georgiev, P. Boolchand, M. Micoulaut, *J. Phys.: Condens. Matter* **2005**, *17*, L1.
[26] P. Boolchand, J. C. Mauro, J. C. Phillips, *Phys. Today* **2013**, *66*, 10.
[27] P. Boolchand, G. Lucovsky, J. C. Phillips, M. F. Thorpe, *Philos. Mag.* **2005**, *85*, 3823.
[28] J. Barré, A. R. Bishop, T. Lookman, A. Saxena, *Phys. Rev. Lett.* **2005**, *94*, 208701.
[29] M. Bauchy, M. J. A. Qomi, C. Bichara, F.-J. Ulm, R. J.-M. Pellenq, *Phys. Rev. Lett.* **2015**, *114*, 125502.
[30] I. Pignatelli, A. Kumar, R. Alizadeh, Y. L. Pape, M. Bauchy, G. Sant, *J. Chem. Phys.* **2016**, *145*, 054701.
[31] M. Bauchy, M. Wang, Y. Yu, B. Wang, N. M. A. Krishnan, E. Masoero, F.-J. Ulm, R. Pellenq, *Phys. Rev. Lett.* **2017**, *119*, 035502.
[32] M. Bauchy, *MRS Bull.* **2017**, *42*, 50.
[33] M. F. Thorpe, P. M. Duxbury, *Rigidity Theory and Applications*, Kluwer Academic/Plenum Publishers, New York **1998**.
[34] J. C. Phillips, M. F. Thorpe, *Phase Transitions and Self-Organization in Electronic and Molecular Networks*, Kluwer Academic/Plenum Publishers, New York **2000**.
[35] M. Micoulaut, M. Popescu, *Rigidity and Boolchand Intermediate Phases in Nanomaterials*, INOE, Bucharest **2009**.
[36] P. Boolchand and M. Micoulaut, *Topology of Disordered Networks and Their Applications*, Frontiers in Materials, Lausanne, Switzerland **2019**.
[37] S. W. King, L. Ross, W. A. Lanford, *J. Non-Cryst. Solids* **2018**, *499*, 252.
[38] A. Malventano, *How 3D XPoint Phase-Change Memory Works*, **2017**, https://pcper.com/2017/06/how-3d-xpoint-phase-change-memory-works/.
[39] G. Lucovsky, J. C. Phillips, P. Boolchand, in *Extended Abstracts of the 2003 Int. Conf. on Solid State Devices and Materials*, Tokyo **2003**, pp. 422–423.
[40] C. Goncalves, M. Kang, B.-U. Sohn, G. Yin, J. Hu, D. T. H. Tan, K. Richardson, *Appl. Sci.* **2018**, *8*, 2082.
[41] S. Raoux, *Annu. Rev. Mater. Res.* **2009**, *39*, 25.
[42] S. Tang, I. V. Karpov, R. Dodge, B. Klehn, J. A. Kalb, J. Strand, A. Diaz, N. Leung, J. Wu, T. Langtry, C. Papagianni, J. Hirst, S. Erra, E. Flores, N. Righos, H. Castro, G. Spadini, in *2009 IEEE International Electron Devices Meeting (IEDM)*, Baltimore, MD, December 2009, pp. 1–4.
[43] P. Boolchand, M. F. Thorpe, *Phys. Rev. B* **1994**, *50*, 10366.
[44] D. G. Georgiev, P. Boolchand, M. Micoulaut, *Phys. Rev. B* **2000**, *62*, R9228.

[45] D. G. Georgiev, P. Boolchand, H. Eckert, M. Micoulaut, K. Jackson, *Europhys. Lett.* **2003**, *62*, 49.

[46] S. Ravindren, K. Gunasekera, Z. Tucker, A. Diebold, P. Boolchand, M. Micoulaut, *J. Chem. Phys.* **2014**, *140*, 134501.

[47] S. Chakravarty, R. Chbeir, P. Chen, M. Micoulaut, P. Boolchand, *Front. Mater.* **2019**, *6*.

[48] K. Gunasekera, S. Bhosle, P. Boolchand, M. Micoulaut, *J. Chem. Phys.* **2013**, *139*, 164511.

[49] R. Chbeir, M. Bauchy, M. Micoulaut, P. Boolchand, *Front. Mater.* **2019**, *6*, 166.

[50] B. S. Almutairi, Badriah Ph.D. thesis, University of Cincinnati, Submitted **2020**.

[51] J. Malek, *Thermochim. Acta* **1997**, *311*, 183.

[52] T. Wagner, S. O. Kasap, M. Vlček, A. Sklenăr, A. Stronski, *J. Mater. Sci.* **1998**, *33*, 5581.

[53] P. Chen, C. Holbrook, P. Boolchand, D. G. Georgiev, K. A. Jackson, M. Micoulaut, *Phys. Rev. B* **2008**, *78*, 224208.

[54] S. K. Sundaram, J. S. McCloy, B. J. Riley, M. K. Murphy, H. A. Qiao, C. F. Windisch, E. D. Walter, J. V. Crum, R. Golovchak, O. Shpotyuk, *J. Am. Ceram. Soc.* **2012**, *95*, 1048.

[55] S. Tsuchihashi, Y. Kawamoto, *J. Non-Cryst. Solids* **1970**, *5*, 286.

[56] J. D. Musgraves, P. Wachtel, B. Gleason, K. Richardson, *J. Non-Cryst. Solids* **2013**, *386*, 61.

[57] Y. Yang, B. Zhang, A. Yang, Z. Yang, P. Lucas, *J. Phys. Chem. B* **2015**, *119*, 5096.

[58] M. Kincl, L. Tichy, *Mater. Chem. Phys.* **2007**, *103*, 78.

[59] T. Qu, P. Boolchand, *Philos. Mag.* **2005**, *85*, 875.

[60] E. Černošková, T. Qu, S. Mamedov, Z. Černošek, J. Holubová, P. Boolchand, *J. Phys. Chem. Solids* **2005**, *66*, 185.

[61] F. Kyriazis, S. N. Yannopoulos, *Appl. Phys. Lett.* **2009**, *94*, 101901.

[62] S. N. Yannopoulos, F. Kyriazis, I. P. Chochliouros, *Opt. Lett.* **2011**, *36*, 534.

[63] D. Th. Kastrissios, G. N. Papatheodorou, S. N. Yannopoulos, *Phys. Rev. B* **2001**, *64*, 214203.

[64] D. R. Lide, G. Baysinger, S. Chemistry, L. I. Berger, R. N. Goldberg, H. V. Kehiaian, *CRC Handbook of Chemistry and Physics*, CRC Press, Boca Raton, FL **2005**.

[65] R. Car, M. Parrinello, *Phys. Rev. Lett.* **1985**, *55*, 2471.

[66] A. Bouzid, C. Massobrio, M. Boero, G. Ori, K. Sykina, E. Furet, *Phys. Rev. B* **2015**, *92*, 134208.

[67] C. Massobrio, M. Micoulaut, P. S. Salmon, *Solid State Sci.* **2010**, *12*, 199.

[68] M. Micoulaut, R. Vuilleumier, C. Massobrio, *Phys. Rev. B* **2009**, *79*, 214205.

[69] C. Massobrio, A. Pasquarello, R. Car, *J. Am. Chem. Soc.* **1999**, *121*, 2943.

[70] M. Bauchy, M. Micoulaut, M. Boero, C. Massobrio, *Phys. Rev. Lett.* **2013**, *110*, 165501.

[71] M. Micoulaut, A. Kachmar, M. Bauchy, S. Le Roux, C. Massobrio, M. Boero, *Phys. Rev. B* **2013**, *88*, 054203.

[72] C. Yildirim, J.-Y. Raty, M. Micoulaut, *Nat. Commun.* **2016**, *7*, 11086.

[73] A. D. Becke, *Phys. Rev. A* **1988**, *38*, 3098.

[74] C. Lee, W. Yang, R. G. Parr, *Phys. Rev. B* **1988**, *37*, 785.

[75] M. Micoulaut, M. Bauchy, P. Boolchand, in preparation (n.d.).

[76] L. Thomas, *Modulated DSC Technology*, TA Instruments, New Castle, DE **2005**.

[77] L. Carpentier, S. Desprez, M. Descamps, *Phase Transitions* **2003**, *76*, 787.

[78] R. A. Robie, P. M. Bethke, *Molar Volumes and Densities of Minerals*, U.S. Geological Survey, Washington **1962**, p. 39.

[79] G. Adam, J. H. Gibbs, *J. Chem. Phys.* **1965**, *43*, 139.

[80] B. G. Aitken, C. W. Ponader, *J. Non-Cryst. Solids* **2000**, *274*, 124.

[81] Y. Yang, Z. Yang, P. Lucas, Y. Wang, Z. Yang, A. Yang, B. Zhang, H. Tao, *J. Non-Cryst. Solids* **2016**, *440*, 38.

[82] S. Dash, P. Chen, P. Boolchand, *J. Chem. Phys.* **2017**, *146*, 224506.

[83] K. S. Andrikopoulos, A. G. Kalampounias, S. N. Yannopoulos, *Phys. Rev. B* **2005**, *72*, 014203.

[84] F. H. Stillinger, T. A. Weber, R. A. LaViolette, *J. Chem. Phys.* **1986**, *85*, 6460.

[85] S. Soyer-Uzun, C. J. Benmore, J. E. Siewenie, S. Sen, *J. Phys.: Condens. Matter* **2010**, *22*, 115404.

[86] S. S. Uzun, S. Sen, C. J. Benmore, B. G. Aitken, *J. Phys.: Condens. Matter* **2008**, *20*, 335105.

[87] S. Chakraborty, P. Boolchand, M. Micoulaut, *Phys. Rev. B* **2017**, *96*, 094205.

[88] M. Bauchy, A. Kachmar, M. Micoulaut, *J. Chem. Phys.* **2014**, *141*, 194506.

[89] R. F. Rowlands, A. Zeidler, H. E. Fischer, P. S. Salmon, *Front. Mater.* **2019**, *6*, 133.

[90] D. G. Georgiev, P. Boolchand, K. A. Jackson, *Philos. Mag.* **2003**, *83*, 2941.

[91] M. Micoulaut, P. Boolchand, *Topology of Disordered Networks and their Applications*, Frontiers – Research Topic, Editorial, **2019**, https://www.frontiersin.org/research-topics/9016/.

[92] S. C. Abrahams, *Acta Crystallogr.* **1955**, *8*, 661.

[93] M. B. Myers, E. J. Felty, *Mater. Res. Bull.* **1967**, *2*, 535.

[94] S. Mamedov, D. G. Georgiev, T. Qu, P. Boolchand, *J. Phys.: Condens. Matter* **2003**, *15*, S2397.

[95] P. Boolchand, J. Grothaus, M. Tenhover, M. A. Hazle, R. K. Grasselli, *Phys. Rev. B* **1986**, *33*, 5421.

[96] F. Wang, S. Mamedov, P. Boolchand, B. Goodman, M. Chandrasekhar, *Phys. Rev. B* **2005**, *71*, 174201.

[97] D. Lathrop, H. Eckert, *Phys. Rev. B* **1991**, *43*, 7279.

[98] Z. Borisova, *Glassy Semiconductors*, Springer US, Boston, MA **1981**.

[99] L. Yan, *Nat. Commun.* **2018**, *9*, 1359.

[100] J. Barré, A. R. Bishop, T. Lookman, A. Saxena, *Phys. Rev. Lett.* **2005**, *94*, 208701.